Mechanical regulation of glycolysis via cytoskeleton architecture

Jin Suk Park[1,2], **Christoph J. Burckhardt**[1,2,*], **Rossana Lazcano**[3], **Luisa M. Solis**[3], **Tadamoto Isogai**[1,2], **Linqing Li**[4,5], **Christopher S. Chen**[4,5], **Boning Gao**[6], **John D. Minna**[6], **Robert Bachoo**[7], **Ralph J. DeBerardinis**[8], **Gaudenz Danuser**[1,2,*]

[1]Lyda Hill Department of Bioinformatics, UT Southwestern Medical Center, Dallas, Texas 75390, USA.

[2]Department of Cell Biology, UT Southwestern Medical Center, Dallas, Texas, USA.

[3]Department of Translational Molecular Pathology, UT MD Anderson Cancer Center, Houston, Texas, USA.

[4]Wyss Institute for Biologically Inspired Engineering at Harvard University, Boston, Massachusetts, USA.

[5]The Biological Design Center and Department of Biomedical Engineering, Boston University, Boston, Massachusetts, USA.

[6]Hamon Center for Therapeutic Oncology, UT Southwestern Medical Center, Dallas, Texas, USA.

[7]Annette G. Strauss Center for Neuro-Oncology, UT Southwestern Medical Center, Dallas, Texas, USA.

[8]Howard Hughes Medical Institute and Children's Medical Center Research Institute, UT Southwestern Medical Center, Dallas, Texas, USA.

Abstract

The mechanics of the microenvironment continuously modulates cell functions like growth, survival, apoptosis, differentiation, and morphogenesis via cytoskeletal remodeling and actomyosin contractility [1–3]. Although all these processes consume energy [4,5], it is unknown if and how cells adapt their metabolic activity to variable mechanical cues. Here, we report that transfer of human bronchial epithelial cells (HBECs) from stiff to soft substrates causes downregulation of

*Correspondence and requests for materials should be addressed to G.D. christoph.burckhardt@utsouthwestern.edu, gaudenz.danuser@utsouthwestern.edu.

Data availability. Data that support the findings of this study are available within the article and Supplementary Information. Any additional information and related data are available from the corresponding author upon reasonable request. No restriction on data availability applies.

glycolysis via proteasomal degradation of the rate-limiting metabolic enzyme phosphofructokinase (PFK). PFK degradation is triggered by stress fiber disassembly, which releases the PFK-targeting E3 ubiquitin ligase tripartite motif (TRIM)-containing protein 21 (TRIM21). Transformed non-small cell lung cancer cells (NSCLCs), which maintain high glycolytic rates regardless of changing environmental mechanics, retain PFK expression by downregulating TRIM21, and by sequestering residual TRIM21 on a stress fiber population that is insensitive to substrate stiffness. In sum, our data unveil a mechanism by which glycolysis responds to architectural features of the actomyosin cytoskeleton, thus coupling cell metabolism to the mechanical properties of the surrounding tissue. These processes enable normal cells to attune energy production in variable microenvironments, while the resistance of the cytoskeleton to respond to mechanical cues allows high glycolytic rates to persist in cancer cells despite constant alterations of the tumor tissue.

Microenvironments provide active and passive mechanical cues that elicit biochemical signals through mechanotransduction [6]. One such cue is the stiffness of the cell-surrounding material [7]. Cells sense this stiffness primarily through integrin- and cadherin-mediated adhesions that couple the extracellular matrix (ECM) and environment of interacting cells to the actin cytoskeleton [8,9]. Mechanical feedbacks subsequently adjust size, composition and structure of the adhesions, as well as organize the cytoskeleton. These processes are intricately coupled to the activity of intracellular signaling cascades. In the case of integrin-mediated adhesions, for example, the focal adhesion kinase (FAK) regulates diverse downstream signaling pathways, including those promoting cell growth and survival [10]. Increasing substrate stiffness elevates the activity of these pathways in cancer, fibrosis and other diseases [11].

Concurrently, metabolism provides energy and biomass for cellular function and proliferation [12]. Normal cells utilize both glycolysis and oxidative phosphorylation (OXPHOS) in a highly regulated manner to meet their metabolic demands. Cancer cells often display enhanced aerobic glycolysis, presumably to meet the increased metabolic demands of malignancy [13,14]. Recent studies have begun to unveil possible interactions between cell metabolic activities and adhesion and cytoskeletal organization [15–17]. Nonetheless, a direct link between mechanical inputs from the cell environment and metabolic responses remained to be established.

Glycolysis is coupled to cell mechanics

We were curious to examine the interdependence between cell mechanics and metabolism in a system where mechanical strains are well-established regulators of physiological functions. In the lung, human bronchial epithelial cells (HBECs) experience mechanical stimuli with every cycle of respiration [18]. Pulmonary fibrosis and lung cancer increase the stiffness of the ECM and alter the biology and function of both non-transformed and malignant cells [19]. To experimentally modulate the environmental mechanics of HBECs, we plated them on stiff (collagen-coated glass) and soft elastic collagen substrates (storage modulus, G' = 16.1 Pa; loss modulus, G'' = 2.7 Pa; see Extended Data Fig. 1a, b). HBECs extended protrusions on stiff and soft substrates, indicative of mechanical engagement. These cells, however, displayed distinct morphologies in terms of the level of spreading and

formation of actin cables, consistent with high and low states of actomyosin contractility (Fig. 1a) [7]. On both substrates, HBECs maintained viability (Extended Data Fig. 1c). Metabolomic profiles (Extended Data Fig. 1d, e; Supplement table 1) revealed a systematic downregulation of metabolites of glycolysis and the TCA cycle when cells were cultured on soft substrates (Fig. 1b). The accumulation of glucose-6-phosphate coupled with the depletion of downstream intermediates strongly suggested a block in the upper phase of glycolysis. Indeed, both the glycolytic rate (Fig. 1c; Extended Data Fig. 1f) and lactate labeling by ^{13}C-glucose (Extended Data Fig. 1g) declined on soft substrates.

Glycolysis can be controlled by glycolytic enzyme expression [14,20]. While expression of most glycolytic enzymes remained unchanged on soft substrate, all three PFK isoforms, i.e. platelet (P), liver (L), and muscle (M), were downregulated (Fig. 1d; Extended Data Fig. 1h, i). In concordance with the reduced PFK expression, HBECs on soft substrates showed decreased overall PFK activity (Extended Data Fig. 1j). PFK catalyzes a rate-limiting step of glycolysis by phosphorylating fructose 6-phosphate and thus determines the overall glycolytic rate [20,21]. PFK is allosterically regulated by fructose-2,6-bisphosphate (F2,6P), which is synthesized by 6-phosphofructo-2-kinase/fructose-2,6-biphosphatases (PFKFBs) [21]. When cells were conditioned to different substrate stiffness, they retained PFKFB expression, although PFKFB3 was expressed on stiff substrates whereas PFKFB2 was expressed on soft substrates (Extended Data Fig. 1k). Similarly, hexokinase 2 (HK2) and enolase 2 (ENO2) were dominantly expressed in cells on stiff substrates, whereas hexokinase 1 (HK1) and enolase 1 (ENO1) were dominantly expressed in cells on soft substrates (Fig. 1d). Thus, PFK was the only enzyme whose isoforms showed a systematic decrease in expression on soft substrates.

To investigate how PFK expression is mechanically regulated, we focused on PFKP, the most ubiquitously expressed PFK isoform in human tissues [22], including the bronchial epithelium (Extended Data Fig. 1l). We over-expressed GFP-tagged PFKP (PFKP-GFP) in HBEC76. Despite constitutive transcription under a strong CMV promotor, cells on soft substrates showed significantly less PFKP-GFP compared to those on stiff substrate (Fig. 1e, f), suggesting that differential expression of PFKP was post-transcriptionally regulated. Human head and neck epithelial cells also displayed a loss of PFKP expression on soft substrates (Extended Data Fig. 1m).

Given that cancer cells experience variable mechanical conditions during tumorigenesis and metastasis [23], we wondered whether the mechano-responsiveness of glycolysis might play a role in cancer progression. Bulk analysis of differential glycolytic gene expression in lung cancer ranked PFKP as the second most upregulated target after the glucose transporter GLUT1 (Extended Data Fig. 1n). This hinted at the possibility that in tumor tissue the activity of certain glycolytic enzymes is enhanced despite mechanical variation. To test this, we compared the impact of substrate stiffness on glycolysis in non-transformed HBEC3 cells (WT HBEC3) to the impact on HBEC3 cells that were oncogenically transformed by expression of sh-p53, KRAS^{V12}, and c-MYC (mut HBEC3) [24]. Consistent with the mechanical sensitivity of enzyme expression, untransformed HBEC3 showed decreased glycolytic rates when plated on soft substrates (Fig. 1g). Transformed HBEC3, however, maintained glycolytic rates on soft substrates (Fig. 1g). Since their OXPHOS rates were

unaffected by stiffness (Extended Data Fig. 1o), we concluded that mechanical regulation of glycolysis was indeed overridden in these transformed cells. To generalize these findings, we examined a panel of patient-derived NSCLC lines harboring activating mutations in KRAS (HCC4087 and H2009), over-expression of EGFR (H1819), or mutant EGFR (HCC827, deletion of E746 - A750). All tested NSCLC lines retained glycolytic rates (Fig. 1h; Extended Data Fig. 1p) and showed either no or mild change in PFKP expression (Fig. 1i; Extended Data Fig. 1q) on soft substrates. Together, these data establish a link between the mechanical state of the cell environment, PFKP expression and glycolysis in non-transformed cells, whereas this link is inactivated by a variety of oncogenic drivers.

To corroborate our conclusion from *in vitro* cell culture models that oncogenic transformation abrogates the mechano-responsiveness of PFKP expression with *in vivo* data, we performed immunohistochemical analysis of malignant and adjacent healthy lung tissue excised from lung cancer patients. After validating the PFKP antibody in cultured cells (Extended Data Fig. 2a), we implemented a computational pipeline for unbiased classification of normal bronchial, stromal, and tumor tissue compartments and quantification of PFKP expression at the single cell level (Extended Data Fig. 2b, c). Both the bronchial and tumor compartments exhibited higher PFKP expression than stromal compartments apposed or distant to the tumor compartment. Intriguingly, while patches of malignant cells showed homogeneous PFKP levels, normal bronchial tissue displayed steep gradients over distances as short as between neighboring cells (Extended Data Fig. 3a). This supports our findings that while in transformed cells PFKP expression is overall high, the expression levels in untransformed cells are modulated and thus more heterogeneous (Extended Data Fig. 3b, c).

F-actin bundling enhances glycolysis

Because cellular stiffness sensing depends on actomyosin contractility [7], we inhibited myosin II by blebbistatin (Blebb) in untransformed HBEC cells. Indeed, reduced myosin II activity decreased PFKP-GFP intensity (Fig. 2a) and glycolytic rates (Fig. 2b) of HBEC76 on stiff substrates. We also tested whether the downregulation of metabolic efficiency on softer substrates might relate to the damped integrin signaling [25]. Cells seeded in low adhesion dishes had decreased PFKP expression in addition to lower FAK phosphorylation (Fig. 2c). Images of cell morphology and cytoskeleton architecture revealed a striking difference in the organization of actin filaments coupled to integrin anchorage. To quantify these cytoskeleton structural differences we applied steerable filters to extract the length and signal intensity of all curvilinear image features (Extended Data Fig. 4a) [26]. Under low adhesion, cells rounded up with shorter, fragmented filaments (Extended Data Fig. 4b), like unperturbed cells on soft substrates (Extended Data Fig. 4c; compare also Fig. 1a). These analyses confirmed a significant shift from fragmented to bundled actin filament (F-actin) organizations for large cell populations in a given mechanical condition (Fig. 2d, e). Accordingly, we conjectured that PFKP expression and glycolytic rates could be coupled to actin cytoskeleton architecture.

To test this further, we targeted the F-actin structure directly using the actin monomer sequestering compound, latrunculin A (LatA). As predicted, this treatment decreased F-actin

length (Fig. 2f; Extended Data Fig. 4d) and PFKP expression (Fig. 2g). Given that glycolysis was insensitive to mechanical variation in cancer cells, we examined whether F-actin organization was also different between untransformed HBECs and NSCLCs. Compared to HBECs, the actin architecture of NSCLCs included thick peripheral fibers (Extended Data Fig. 4e). Quantification confirmed a mild increase in F-actin length (Extended Data Fig. 4f) and intensity (Extended Data Fig. 4g) in selective NSCLCs compared to untransformed HBECs. To correlate F-actin organization with glycolysis, we again used LatA to disrupt bundled F-actin. Remarkably, glycolytic rates of the KRAS-mutated NSCLC HCC4087 were largely resistant to LatA treatment compared to that of the syngenic HBEC76 cells derived from the same patient (Fig. 2h). This behavior was reproduced in EGFR-mutated NSCLC HCC827 cells (Fig. 2h). OXPHOS rates were relatively unaffected by LatA in both NSCLCs and HBECs, suggesting again the specificity of modulation in actin cytoskeleton architecture towards glycolysis (Extended Data Fig. 4h). In line with our hypothesis that higher glycolytic rates are related to the presence of thick F-actin structures, images of HCC4087 before and after LatA treatment showed that the characteristic peripheral fibers were retained (Fig. 2i). These fibers were also retained between HCC4087 cultured on stiff and soft substrates (Fig. 2j). Thus, our data show a sensitivity of the actin cytoskeleton to environmental mechanical changes or to actin monomer sequestration in untransformed cells, which regulates glycolysis. This sensitivity is absent in transformed NSCLCs, allowing these cancer cells to stabilize glycolysis in the face of variable mechanical cues.

Mechanical regulation of phosphofructokinase degradation by E3-ligase TRIM21

Since PFKP is post-transcriptionally regulated (Fig. 1e), we hypothesized that the link between environmental mechanics, actin cytoskeleton architecture, PFKP expression, and glycolysis should relate to the rate of PFKP degradation. To test this, we pulse-labeled PFKP with L-azidohomoalanine in human embryonic kidney 293 (HEK) cells and followed protein degradation for 24 hrs (Extended Data Fig. 5a). In the presence of proteasome inhibitor, MG132, endogenous PFKP expression was increased (Extended Data Fig. 5b). By pulling down ubiquitin-conjugated proteins, we then observed PFKP polyubiquitination (Extended Data Fig. 5c), which was enhanced by MG132 (Extended Data Fig. 5d). Thus, PFKP undergoes proteasome-mediated degradation, as reported before [27]. In line with this finding, acute inhibition of the proteasome in HBECs rescued PFKP expression on soft substrates (Fig. 3a).

Protein ubiquitination occurs primarily on lysine residues [28]. Mutating these lysines disrupts ubiquitination and enhances protein abundance. We therefore tested whether lysine-to-arginine mutations would block the decrease in PFKP-GFP expression on soft substrates (Extended Data Fig. 5e). Among nine tested residues, the K281R mutation strongly desensitized HBEC76 cells from mechano-responsive PFKP degradation (Fig. 3b; Extended Data Fig. 5f-m). Structural analysis showed that K281 is a highly exposed residue suitable for intermolecular interactions (Extended Data Fig. 5n, o) and HBEC76 cells expressing this mutant form of PFKP largely resisted the inhibitory effect of soft substrates on glycolysis (Fig. 3c). Mutagenesis of the equivalent lysine residues in PFKL (K272R) and in PFKM

(K275R) reduced PFKL degradation and rescued PFKM expression (Extended Data Fig. 5p, q, respectively), reaffirming a conserved regulation of all three PFK isoforms by mechanical inputs (Extended Data Fig. 6).

Proteasome-mediated degradation is facilitated by E3 ubiquitin ligases that conjugate ubiquitin to targeted proteins [28]. Decreasing the activity or the expression of E3 ligases hinders ubiquitination and thus prevents degradation of target proteins. While previous work has established the E3 ligase TRIM21 as targeting PFKP for proteasomal degradation [27], we compiled a broader set of potential PFKP-modulating ligases from the list of E3 ubiquitin ligases with systematic downregulation in lung cancer. Although the effect was fairly mild, TRIM21 was the second most consistently downregulated E3 ligase when scoring 20 datasets from the Lung Cancer Explorer (LCE; Extended Data Fig. 7a) [29]. We then performed a knock-down screen of 18 ligases and identified TRIM21 as the only knockdown target that enhanced PFKP expression (Extended Data Fig. 7b). Confirming our conclusion from experiments in an untransformed HBEC line, we observed lower TRIM21 expression in the panel of NSCLCs employed in this study (Extended Data Fig. 7c). Thus, we focused on TRIM21 to further elucidate the mechanisms of the putative link between F-actin architecture and PFKP degradation.

We first confirmed in HEK cells that overexpression of GFP-tagged TRIM21 (TRIM21-GFP) led to accumulation of polyubiquitinated PFKP (Extended Data Fig. 7d). Moreover, shRNA-mediated knockdown of TRIM21 (shTRIM21) in untransformed HBECs was sufficient to increase PFKP expression on stiff substrates, and to reduce PFKP degradation on soft substrates (Fig. 3d). Conversely, overexpression of TRIM21-GFP in these cells decreased PFKP expression when cells were plated on stiff substrates (Fig. 3e). Corroborating these data, in NSCLC cells on stiff substrates TRIM21 knockout by CRISPR increased PFKP expression (Extended Data Fig. 7e) and overexpression of TRIM21-GFP decreased PFKP expression (Fig. 3f). Thus, manipulation of TRIM21 expression in untransformed and transformed lung epithelial cells alters PFKP expression. Although AKT-mediated phosphorylation has been reported to protect PFKP from TRIM21-mediated ubiquitination [27], PFKP expression remained unchanged upon AKT inhibition (Extended Data Fig. 7f). When we over-expressed PFKP-GFP harboring a mutation (S386A) that blocked phosphorylation by AKT, we did not observe an enhanced decrease in PFKP expression on soft substrate (Extended Data Fig. 7g), indicating that mechanically modulated PFKP expression in HBECs was independent of AKT signaling. Importantly, TRIM21 expression itself was unaffected by substrate stiffness (Fig. 3d, e). Thus, if TRIM21 were indeed involved in regulating the mechano-responsiveness of glycolysis, its function would be related directly to F-actin organization.

F-actin bundles inhibit TRIM21 function by sequestration

To explore a connection between F-actin organization and TRIM21's ligase function, we returned to our previous insight that transformed NSCLCs maintained equally thick actin bundles on stiff and soft substrates (Fig. 2j) and maintained equal levels of PFKP expression (Extended Data Fig. 1q). Combining these two mechanical invariants, we suspected an association between TRIM21 and F-actin. Indeed, we observed a strong co-localization of

TRIM21 and F-actin in NSCLC cells (Fig. 4a; Extended Data Fig. 8a). Although untransformed HBEC76 showed relatively weak F-actin bundles even when plated on stiff substrates, co-localization between TRIM21 and F-actin was apparent also under these conditions (Extended Data Fig. 8b). To corroborate the dependence of TRIM21 localization on F-actin structure, we enhanced stress fiber formation in HBEC76 by treatment with lysophosphatidic acid (LPA), which activates RhoA signaling and actomyosin contractility. Strikingly, these biochemical manipulations not only increased the concentrated localization of TRIM21 to prominent F-actin bundles, but reduced the background of diffuse, cytosolic TRIM21 (Extended Data Fig. 8b), suggesting that binding to F-actin may limit the mobility and thus the radius of action of TRIM21 as a ligase. This model would also explain why thick F-actin bundles in NSCLC cells, regardless of substrate stiffness, resulted in persistent PFKP expression and glycolysis. The interaction between TRIM21 and F-actin was further verified by an actin co-sedimentation assay in HEK cell lysates (Fig. 4b). Subsequently, we performed a mass spectrometry screen and found actin and actin cross-linking alpha-actinin, which localizes to contractile stress fibers, among TRIM21's strongest binding partners (Supplementary table 6). Thus, we concluded that TRIM21's function as a PFKP-targeting ligase is, at least in part, modulated by sequestration of the ligase to F-actin bundles.

To test the hypothesis that PFKP expression and glycolysis are related to the abundance of thick, TRIM21-sequestering F-actin bundles, we directly manipulated F-actin architecture by expression of the phosphomimetic alpha-actinin 1 (ACTN1^{Y246E}). This mutant has been previously reported as a strong F-actin bundling factor [30], and the tyrosine residue Y246 also has been identified as a downstream effector of oncogenic signaling [31,32]. Compared to the expression of GFP alone or GFP-labelled, wildtype alpha-actinin 1 (ACTN1-GFP), the expression of ACTN1^{Y246E}-GFP resulted in strong actin bundles in HBEC76 (Extended Data Fig. 8c) and HEK cells (Extended Data Fig. 8d), akin to the F-actin bundles observed in NSCLCs. Indeed, by manipulating F-actin structures, these cells were able to sequester overexpressed TRIM21-GFP (Extended Data Fig. 8e, f). When seeded on soft substrates, these cells also maintained enhanced actin bundles (Fig. 4c). Thus, cells were able to maintain PFKP expression and glycolysis even on soft substrates (Fig. 4d, e; Extended Data Fig. 8g).

Many cancers harbor proteins with conserved cysteine residues mutated in the RING domain of E3 ligases (Supplement table 2; Extended Data Fig. 9a-e) [33,34]. In TRIM21, the cysteine residue at site 54 was substituted by tyrosine in one patient (C54Y) (Supplement table 5; Extended Data Fig. 9a). Following this lead, we discovered that when expressed in HBEC76, TRIM21^{C54Y} led to perinuclear aggregation (Extended Data Fig. 9f). Besides the C54Y mutation, other cysteine mutations in the RING domain of TRIM21 showed similar aggregation (Extended Data Fig. 9g) while non-cysteine mutations of TRIM21 reported in TCGA did not (Extended Data Fig. 9h). This points to aggregation as a conserved mechanism of inactivation of RING domain proteins in cancer and offers a mechanism in parallel to cytoskeleton-based sequestration for the inactivation of TRIM21. Indeed, overexpression of TRIM21^{C54Y}-GFP affected neither PFKP expression (Extended Data Fig. 9i) nor glycolysis rates (Extended Data Fig. 9j compared to HBEC76 in Fig. 1c, dotted line) on stiff substrates, indicating that C54Y impaired TRIM21's ligase function.

In summary, our data establish a mechanism for mechanically regulated glycolysis through TRIM21-modulated degradation of PFKP. F-actin bundling and stress fiber formation spatially sequester the E3 ligase TRIM21, thus reducing its access to substrates such as PFKP. As a result, glycolysis remains high. Under mechanical conditions that permit relaxation of the actomyosin cytoskeleton the ligase is released, PFKP is degraded, and thus glycolytic rates are reduced. In transformed cells, mechano-responsiveness of glycolysis is bypassed by an F-actin architecture of thick bundles that resist changes in extracellular mechanical cues. The high tendency of TRIM21 inactivation by sequestration regardless of environmental factors is, at least in some lung cancers, supported by lower expression of the ligase. Together, this reduces PFKP degradation and yields a consistently high expression of this rate-limiting glycolytic enzyme. In addition, cancer-related loss of function mutations of TRIM21 form aggregates that also block access of the ligase to its targets. Thus, the control of protein degradation via sequestration of E3 ligases may be a widespread motif of physiological proteostasis that becomes altered in disease [35]. In cancer cells, suppressing TRIM21 function may result in the metabolic hallmark of persistent glycolysis withstanding heterogeneous mechanical environments.

METHODS

Cell lines, culture and reagents.

All CDK4/hTERT-immortalized normal HBECs (3, 30, 34, and 76), and NSCLC cell lines (HCC4087, H2009, HCC827, and H1819) were generated in the Hamon Center for Therapeutic Oncology (UT Southwestern Medical Center, Dallas, TX). The fully transformed, mutant HBEC3 (Mut HBEC3) was previously established by expressing sh-p53, KRAS^{V12}, and c-MYC [24]. HBEC76 and HCC4087 were generated from the same patient. HBECs were maintained in keratinocyte serum-free medium (KSFM; 17005042, Thermo Fisher Scientific, Waltham, MA) supplemented with human recombinant Epidermal Growth Factor 1–53 (EGF, 5 ng/mL, Gibco) and Bovine Pituitary Extract (BPE, 50 mg/mL, Gibco), and NSCLCs were maintained in RPMI-1640 (11875–085, Gibco) and 5% fetal bovine serum (FBS, F0926, Sigma-Aldrich, St. Louis, MO). All lung cell lines were cultured at 37°C with antibiotic-antimycotic (Anti-Anti, 15240–062, Gibco) in a humidified incubator with 5% CO_2, and were routinely tested for mycoplasma contamination using MycoScope PCR detection kit (MY01050, Genlantis, San Diego, CA). Upon trypsinization, cells were treated with trypsin neutralizer solution (R002100, Gibco) and centrifuged before they were re-suspended in fresh media.

Stiff substrates were generated by coating tissue culture dishes with bovine collagen type I (PureCol, Advanced BioMatrix, Carlsbad, CA). When coating, a sufficient amount of diluted collagen solution (50 μg/mL in PBS) was added to fully cover the surface of a culture dish before incubating it for 1 hr at 37°C. The remaining solution was aspirated, and the dish was rinsed with PBS before seeding cells. Soft substrates were generated by polymerizing a bovine collagen type I gel (PureCol, 2.5 mg/mL; Advanced BioMatrix) on a 50 mm glass-bottom dish (MatTek, Ashland, MA). A collagen gel solution was made by mixing 8 parts of chilled collagen solution with 1 part of 10X PBS and 1 part of NaOH (0.1 N) or by adjusting the pH of the mixture to approximately 7 as indicated by pH paper. The

mixture was added to the glass-bottom section of the dish, and incubated for 1 hr or until completion of the gelation at 37°C. Cells were then seeded at 5×10^5 cells in 1 mL of culture media directly on top of the gels. Additional culture media were added once cells were attached to the gels, and cells were incubated for 24 hrs before performing an experiment. When collecting cells from soft substrates, cells were first washed with pre-warmed Hank's Balanced Salt Solution (HBSS, Thermo Fisher Scientific) and collagen gels were digested using pre-warmed collagenase type I (1U in HBSS, Gibco) for 20 min at 37°C. When inhibiting integrin anchorage, cells were seeded in low adhesion dishes (Corning) for 24 hrs and compared to adherent cells in tissue culture-treated dishes.

For pharmacological perturbations, cells were treated with AKT inhibitor X (124020; Sigma-Adrich), blebbistatin (B0560; Sigma-Aldrich), latrunculin A (ab144290; Abcam), MG132 (A2585; APExBIO), lysophosphatidic acid (CAS 325465–93-8; Santa Cruz) or equivalent concentration of DMSO as control for 24 hrs unless stated otherwise. Cells were treated for 15 hrs with AKT inhibitor X which was refreshed every 3 hrs. For experiments using lysophosphatidic acid (20 μM), cells were treated for 30 min before applying additional manipulations.

For TRIM21 KO, H2009 cells were transfected with the gRNA-wtCas9–2A-GFP plasmid targeting the first exon of TRIM21 using the NEON electroporation system (Thermo Fisher) according to manufacturer's protocols. In brief, cells were trypsinized, washed once with PBS, counted with a Cellometer Auto 1000 (Nexcelon Biosciences, Lawrence, MA) and resuspended at 5×10^6 cells/mL in PBS. Cells were mixed with 80 μg/mL plasmid DNA and electroporated in 100 μL electroporation tips for two pulses at 1230 V for 30 ms and brought back into culture medium. After expansion, single GFP positive cells were sorted into 96 well plates with a FACS Aria II SORP flow cytometer (Beckton Dickinson) in culture medium. Cell clones were expanded and tested for TRIM21 expression by western blotting as described below.

Over-expression and knockdown constructs and virus packaging.

For the constitutive expression of GFP tagged fusion constructs, human cDNA clones from the Ultimate ORF library (Thermo Fisher Scientific, Waltham, MA) were obtained from the UT Southwestern McDermott Center Sequencing Core facility for PFKP (ID: IOH4086), PFKM (IOH3708), PFKL (IOH6888) and TRIM21 (IOH9948), ACTN1 (IOH4989). The cDNAs were amplified with forward and reverse oligonucleotides (IDT DNA, Coralville, IA) as listed in supplement table 3 by PCR using PfuUltra II Fusion HS DNA polymerase (600674, Agilent Technologies, Santa Clara, CA) on a C1000-Touch thermal cycler (Bio-Rad, Hercules, CA). Products were subjected to electrophoresis on 1% agarose gels, extracted from gels and purified on spin columns (MB082, Sydlabs, Natick, MA) according to manufacturer's instructions. For fusion protein over-expression, pEGFP-N1(6085–1, Clontech, Mountain View, CA), with the A206K mutation that was shown to reduce GFP oligomerization [38] was used. Expression was driven by a human cytomegalovirus immediate early promotor (hCMV). The PCR fragments were subcloned into pEGFP-N1 using EcoRI (R3101S, all restriction enzymes from New England Biolabs, Ipswich, MA) and BamHI (R3136S) for PFKP, XhoI (R0146S) and BamHI for PFKM, XhoI and EcoRI for PFKL,

EcoRI and KpnI (R3142S) for TRIM21, and EcoRI and KpnI for ACTN1. Digested vector was dephosphorylated with calf intestine phosphatase (M0290, NEB) and vector and fragments were agarose gel purified and ligated with T4 DNA ligase (M0202, NEB) at 16°C for 1 hr. Products were transformed into XL-1 blue Ecoli cells (200130, Agilent Technologies) according to standard protocols and spread on kanamycin (BP906–5, Fisher Scientific) selective agar plates. Colonies were expanded, plasmid DNA was extracted using standard protocols and spin columns (Sydlab) and clones verified by restriction digest analysis on 1% agarose gels. To introduce the TRIM21 C54Y mutation, oligonucleotides including single nucleotide changes (Supplement table 3) were used for PCR amplification of pEGFP-TRIM21-GFP with PFU ultra II polymerase according to standard site directed mutagenesis procedures. Input DNA was digested by DpnI (R0176, NEB) at 37°C, samples were purified over spin columns, transformed into XL-1 blue cells and plated on kanamycin selective plates. Resulting clones were sequence verified by Sanger sequencing (Genewiz, South Plainfield, NJ). The same procedures were used to introduce other point mutation (for oligonucleotides see supplement table 3). For lentiviral expression, PFKP-GFP, TRIM21-GFP, and ACTN1-GFP were subcloned from pEGFP vectors into pLVX puro or neo (632183, 832181, Clontech) vectors using SnaBI (R0130, NEB) and NotI (R3189S) restriction sites. For shRNA mediated protein knockdown vectors from the pGIPZ lentiviral library (Dharmacon, Lafayette, CO) were used (see supplement table 4 for sequences), where expression is driven by hCMV promotor and an internal ribosomal entry site allows GFP, puromycin or neomycin resistance gene and shRNA expression from the same transcript. As a control pGIPZ shRNA empty vector was used. For the TRIM21 KO, a Crispr/Cas9 approach was used following established protocols [39]. The DNA sequence of the first exon of the human TRIM21 gene was retrieved from the Ensembl genome browser (http://www.ensembl.org) [40] and subjected to a gRNA guide selection algorithm (http://crispr.mit.edu/). The sequence 5'-GAAACACCGTGACCACGCCA –3' obtained high scores and oligonucleotides (IDT DNA) were designed for cloning into pSpCas9(BB)-2A-GFP (PX458, Addgene 48138, the plasmid was a gift from Feng Zhang, Massachusetts Institute of Technology, Cambridge, MA). In brief, oligonucleotides were phosphorylated with T4 polynucleotide kinase (M0201, NEB) for 30 min at 37°C, heated to 95°C and annealed by slow cool down in the thermal cycler (Bio Rad). The vector was digested with BbsI (R0539, NEB) and purified on a 1% agarose gel as described above. Oligonucleotide dimers and digested vector were ligated using T4 DNA ligase as described above and unligated plasmid DNA was digested with plasmid safe ATP dependent DNAse (E3105K, Epicentre, Madison, WI), including 1 mM ATP for 30 min at 37°C followed by 10 min heat inactivation of the enzyme at 70°C. The DNA was transformed and cells spread on ampicillin (A-301–10, Goldbio, St. Louis, MO) selective plates as described above. Resulting clones were verified by Sanger sequencing as described above. Selected plasmids were deposited at Addgene.

For virus packaging of pLVX GFP fusion constructs and for pGIPZ lentiviral shRNA constructs, psPAX2 and pMD2.G were used (Addgene #12260 and #12259, respectively), plasmids were a gift from Didier Trono (EPFL Lausanne, Switzerland). For lentivirus production, human embryonic kidney cells (gift from Hyeryun Choe, The Scripps Research Institute, Scripps Florida) were transfected with expression and packing plasmids following

standard calcium-phosphate or polyethylenimine (Polysciences, 23966) protocols, supernatant was collected two-days post transfection, filtered through 0.45 μm mixed cellulose esters membrane syringe filters (09–720-005, Fisher Scientific) and incubated on HBEC and cancer cells in the presence of 2 μg/mL polybrene (TR-1003-G, Millipore, Burlington, MA). After multiple days of expression and cell expansion, GFP positive cells were collected on a FACS Aria II SORP flow cytometer equipped with a 488 nm laser (Beckton Dickinson, Franklin Lakes, NJ) and returned to culture. For pGIPZ knockdown cells, protein expression was assessed by western blotting as described below.

Collagen hydrogel mechanical characterization.

The mechanical properties of collagen hydrogels were measured using a strain-controlled Discovery HR-2 (DHR-2) oscillatory shear rheometer (TA Instruments, New Castle, DE), with a 50-mm diameter cone-on plate geometry, 1° cone angle and a 200 μm gap distance at 37°C [36]. The collagen solution was prepared and pH-adjusted, approximately to 7, to reach a final concentration of 2.5 mg/mL following the same protocol described above. Collagen precursor solution (1mL) was deposited onto the rheometer peltier plate (chilled at 4°C) for in situ mechanical stiffness measurements. To determine hydrogel formation and gelation kinetics, the temperature was increased from 4°C to 37°C over 5 seconds to initiate hydrogel formation. It was followed by an oscillation time step for 60 minutes performed at a constant 1 Hz frequency and 1% strain amplitude at 37°C to confirm the liquid-to-solid transition and to record hydrogel stiffness. To assess the stiffness of preformed collagen hydrogels, precursor solutions (1 mL) were first incubated at 37°C for one hour before initiating the 60-min oscillation time step at 1 Hz frequency and 1% strain amplitude. Frequency steps were also conducted over a logarithmic scale from 0.1 Hz to 10 Hz at a fixed strain amplitude of 1% to test the mechanical stability of the resulting hydrogels. Shear moduli (Pa) of resulting hydrogels were recorded in storage modulus (G') as indicative of the elastic component and in loss modulus (G'') as indicative of the viscous component of the material. For consistency, the characterization of the mechanical properties of collagen hydrogels adapted the identical hydrogel platform that was employed for cell culture with regards to hydrogel volume, diameter, pH and temperature. The stability of hydrogels was assessed based on the ratio G'/G'' (~6 in our case), where a higher fold difference indicates elastic behavior of stable hydrogels. Data were collected from multiple independent measurements as indicated in the text.

Metabolomics.

HBEC76 were plated at 1×10^6 cells per 60-mm dish for stiff substrates or 50-mm glass-bottom dish for soft substrates and incubated for 24 hrs. Cells on stiff substrates were scraped and collected once they were washed with ice-cold saline and lysed with ice-cold 80% methanol in water. Cells on soft substrates were collected after collagen gels were digested with collagenase as described above. They were centrifuged and pelleted at 4°C, washed with ice-cold saline, and pelleted again before they were lysed with ice-cold 80% methanol in water. All lysed samples were scraped into Eppendorf tubes followed by three freeze-thaw cycles in liquid nitrogen before they were centrifuged and pelleted at 4°C. The supernatant was collected and dried in an Eppendorf tube using a SpeedVac concentrator (Savant, Thermo Fisher Scientific). Metabolites were rehydrated in 100 μL of 0.03% formic

acid (85178, Thermo Fisher Scientific) in LCMS-grade water (51140, Thermo Fisher Scientific), and centrifuged after vortex-mixed to remove debris. The supernatant was transferred to a high-performance liquid chromatography (HPLC) vial, and metabolite profiling was determined by liquid chromatography-tandem mass spectrometry (LC-MS/MS). An AB QTRAP 5500 liquid chromatography/triple quadrupole mass spectrometer (Applied Biosystems SCIEX) was used to perform LC-MS/MS and data acquisition as previously described [41]. MultiQuant software version 2.1 (Applied Biosystems SCIEX) was used for chromatogram review and peak area integration. The peak area for each metabolite was normalized to the total ion count of that sample (Supplement table 1), and the normalized data were auto-scaled (mean-centered and divided by the standard deviation of each variable) using MetaboAnalyst 4.0 (www.metaboanalyst.ca) [42]. Univariate statistical differences of the metabolites between two groups were analyzed using a two-tailed Student's *t*-test.

Isotope-labeling experiment.

Isotope-labeling experiments were performed in reference to the previous study [43]. In summary, KSFM was supplemented with isotopically labeled D-[U-^{13}C]-glucose (7 mM; CLM-1396, Cambridge Isotope Laboratories). HBEC76, seeded on either stiff or soft substrates, were incubated with the labeled media for 1 hr before they were washed with ice-cold saline and collected with ice-cold 50% methanol in water. Following three freeze-thaw cycles, cell lysates were centrifuged and the supernatant was air-dried after adding an internal standard (20 nmol of norvaline). The extracted metabolites were re-suspended in anhydrous pyridine and incubated with N-(tert-butyldime-thylsilyl)-N-methyltrifluoroacetamide (MTBSTFA) derivatization reagent for 1 hr at 70°C. Once transferred to an autoinjector vial, metabolites were analyzed based on the validated retention times and mass fragmentation signatures using either an Agilent 6890 gas chromatograph coupled to an Agilent 5973N mass selective detector or 7890 gas chromatograph coupled to an Agilent 5975C mass selective detector. Once corrected for natural abundance, the mass isotopologue distribution was determined. GC/MSD ChemStation Software (Agilent) was used for chromatogram review and peak area integration. The peak area for each metabolite was normalized to the total ion count of that sample. The abundance of each mass istopomer was shown as a fraction of the total pool. Univariate statistical differences of the metabolites between two groups were analyzed using a two-tailed Student's *t*-test.

Seahorse assay.

The assay was performed according to the manufacturer's instruction. Briefly, a day before the experiment, a Seahorse cartilage (100850–001, Agilent Technologies) was hydrated and incubated at 37°C without CO_2. Cells were seeded at 4×10^4 cells/well to a Seahorse 24-well plate (100777–004, Agilent Technologies) and incubated overnight at 37°C. To examine cells on different substrate stiffness, Seahorse XF24 Islet Capture Microplates (101122–100, Agilent Technologies) were used. The microplates were either coated or filled with 10 μL of collagen gel mixtures before cells were seeded, as described above. To test the effect of latrunculin A (LatA), the seeded cells were incubated overnight with the stated concentration of LatA for at 37°C. On the day of experiment, the Seahorse XFe24 analyzer

(Agilent Technologies) was calibrated using the hydrated cartilage. Cells were washed with PBS, and the culture medium was changed to sodium bicarbonate-free, FBS-free DMEM that contained 5.5 mM glucose (D2902, Sigma-Aldrich) of which the pH was calibrated to 7.3 – 7.4 using sodium hydroxide. For cells in Islet Capture Microplates, islet capture screens were hydrated in culture media to remove any air bubbles, and were inserted into each well using a capture screen islet tool (101135–100, Agilent Technologies). After incubating cells for 1 hr at 37°C, the Seahorse assay was performed by measuring the extracellular acidification rates (ECAR) as a proxy for glycolytic readouts and the oxygen consumption rates (OCR) as a proxy for oxidative phosphorylation readouts. The data was acquired and analyzed using Wave Controller 2.4 software (Agilent Technologies).

Fluorescence microscopy, image analysis and statistics.

To assess F-actin organization and TRIM21 distribution, cells were seeded on #1.5 cover glass (2850–22, Corning, Corning, NY) coated with fibronectin. In brief, cells were fixed with 4% paraformaldehyde (P6148, Sigma) in phosphate buffered saline (PBS) for ten minutes, washed and permeabilized with 0.5% Triton-X100 (BP151, Fisher) in PBS for five minutes. Cells were washed with PBS, blocked in PBS containing 5% goat serum (16210064, Thermo) for one hour at room temperature. Cells were washed and incubated with Alexa-Fluor-568 conjugated phalloidin (A12380, Thermo Fisher Scientific) for 15 minutes at 4°C. Cells were washed again and mounted with Vectashield antifade mounting medium (H-1000, Vector Labs, Burlingame, CA) for microscopy.

For fluorescence microscopy, fixed and stained cells were imaged on an eclipse-Ti inverted epifluorescence microscope with a Plan Fluor 40× 1.30NA oil objective (Fig. 1a, e, 2a, Extended Data Fig. 1c) or a Plan Apo λ 100× 1.45NA oil objective (Nikon) (Fig. 2i, j, 4c, Extended Data Fig. 4b, c, d, e, 8b-f, 9f-h), a Lambda-XL light source and Lambda 10-B smart shutter (Sutter Instruments, Navato, CA). Images were acquired with a Zyla sCMOS camera (Andor) and the microscope was controlled using μManager [44]. For figure 1a, F-actin was stained with Alexa-Fluor-568 conjugated phalloidin (A12380, Thermo Fisher Scientific) and the nuclei were stained with Hoechst 33342 (H1399, Thermo Fisher Scientific). When quantifying PFKP-GFP intensity as shown in figures 1e and 2a, HBEC76 expressing PFKP-GFP were imaged at stated experimental conditions. Average intensity of PFKP-GFP per cell after subtraction of the global image background was determined in manually segmented cell contour, and using ImageJ 1.51w software [45]. For figure 4a, Extended Data Fig. 8a, slides were analyzed on a TI-eclipse inverted microscope (Nikon), equipped with an Apo TIRF 60× 1.49NA objective with a 1.8x tube lens yielding 108x magnification and Discovery Platform spinning disc and TIRF units (Andor, Concord, MA). Images were recorded with a Zyla sCMOS camera (Andor) controlled by Metamorph 7.8.13.0 software (Molecular Devices, San Jose, CA).

To normalize the Seahorse data with cell number, cells were stained with Hoechst 33342 (1 μg/mL, H1399, Thermo Fisher Scientific) and incubated for 20 min at 37°C. Cells were then analyzed on an eclipse-Ti inverted microscope with Plan Fluor 4× 0.13NA objective and a motorized stage (Nikon), with X-cite 120 LED light source (Lumen Dynamics). Images were acquired as 2 × 2 stitched fields with 10% overlaps to fully capture the area of a single

well using a Zyla sCMOS camera (Andor) controlled by Nikon Elements software. The inner area of each well was cropped out from the images, and cell numbers were counted by determining the number of local fluorescence maxima using ImageJ [45]. A noise tolerance value was set to threshold the fluorescence signals and to avoid false positive signals from the background.

Actin filament images were analyzed applying a steerable filter approach with previously described and deposited software [26]. In brief (see also Extended Data Fig. 4a), first, features were enhanced by multi-scale steerable filtering and centerlines of curvilinear features were extracted. Next, the filament fragments were classified into high and low confidence and a graph matching was applied to connect the fragments. This procedure yielded filament positions as chains of connected pixels. From the detected filaments, the length and pixel intensity parameters were determined using customized scripts written in Matlab 2018a (The Mathworks, Natick, MA). Filaments were shown as binary images. For visualization, filament thickness was enhanced by dilation using ImageJ [45].

Cell viability.

Cell viability was assessed using a LIVE/DEAD Viability/Cytotoxicity Assay Kit (L3224, Thermo Fisher Scientific). Live cells were stained with 2 μM Calcein AM while dead cells were stained with 4 μM Ethidium homodimer for 20 min at 37°C. Cells were then imaged by fluorescence microscopy and analyzed using ImageJ [45]. Viability was quantified per image as the fraction of Calcein AM positive cells among all cells. The total number of cells was calculated by adding a number of live cells and a number of dead cells.

PFK activity analysis.

PFK activity was assessed using a 6-Phosphofructokinase Activity Assay Kit (ab155898, Abcam) based on the manufacturer's instruction. In summary, HBEC76 were cultured on stiff and soft substrates, respectively, and then harvested in Cell Lysis Buffer (9803, Cell Signaling) supplemented with Halt Protease and Phosphatase Inhibitor Cocktail (78442, Thermo Fisher Scientific) as stated above. Standard curves were generated from NADPH prepared from 0 to 10 nmol/well. PFK reaction mixes were assembled in a 96-well plate by mixing cell lysates with Assay Buffer, PFK Developer, ATP, and PFK substrate as provided in the kit. The PFK reactions were monitored in a kinetic mode for 1 hr at 5 min intervals using a microplate reader (Synergy-H1, BioTek, Winooski, VT) that measured absorbance at OD 450 nm at 37°C. Two time points within the linear growth phase of absorbance were selected to calculate PFK activity as suggested by the manufacturer.

Immunoblotting and immunoprecipitation.

Protein lysates were prepared in ice-cold RIPA buffer (R0278, Sigam-Aldrich) supplemented with Halt Protease and Phosphatase Inhibitor Cocktail (78442, Thermo Fisher Scientific). Cells were mechanically ruptured by pressing them through a PrecisionGlide needle (305109, BD, Franklin Lakes, Nj) for at least five times. After one freeze-thaw cycle in liquid nitrogen, lysates were centrifuged and pelleted at 4°C. The supernatant was collected and quantified using the BCA protein assay (23228, Thermo Fisher Scientific) analyzed on a microplate reader (Synergy-H1, BioTek, Winooski, VT) at 562 nm absorbance

with Gen5 software (BioTek). Samples were diluted in a Laemmli sample buffer (161–0747, Bio-Rad, Hercules, CA) with 2-mercaptoethanol (BP176, Fisher) and boiled for 5 min. Proteins were separated on 7.5% SDS-PAGE gels (456–8024, Bio-Rad) and transferred to nitrocellulose membranes (88018, Thermo Fisher Scientific) using a Trans-Blot Turbo Transfer System (Bio-Rad). Once membranes were blocked with 5% bovine serum albumin (BSA, BAH65–0500, Equitech-Bio, Kerrville, TX) in Tris buffered saline (TBS) with 0.1% Tween 20 (TBST, BP337, Fisher) for 1 hr at room temperature, they were probed with antibodies against HK1 (C35C4, Cell Signaling, Danvers, MA), HK2 (C64G5, Cell Signaling), PFKP (D4B2, Cell Signaling), PFKL (8175, Cell Signaling), PFKM (55028–1-AP, Proteintech, Rosemont, IL), ALDA (D73H4, Cell Signaling), GAPDH (D16H11, Cell Signaling), PGAM1 (D3J9T, Cell Signaling), ENO1 (3810, Cell Signaling), ENO2 (D20H2, Cell Signaling), PKM½ (C103A3, Cell Signaling), LDHA (C4B5, Cell Signaling), PDH (C54G1, Cell Signaling), β-actin (A1978, Sigma-Aldrich), PFKFB2 (D7G5R, Cell signaling), PFKFB3 (D7H4Q, Cell Signaling), pFAK (Y397, 3283, Cell Signaling), FAK (3285, Cell Signaling), Ubiquitin (P4D1, Cell Signaling), TRIM21 (D1O1D, Cell Signaling), alpha actinin-1 (ab18061, abcam), and GFP (11814460001, Roche) in 5% BSA in TBST for overnight at 4°C. The specificity of PFK isoform antibodies was verified on protein samples expressing GFP-fusion constructs (Extended Data Fig. 1i). Membranes were washed with TBST, probed with secondary antibodies conjugated with horseradish peroxidase (goat anti mouse: 115–035-003, goat anti rabbit: 111–035-003, Jackson ImmunoResearch, West Grove, PA). Once they were washed again, bands were detected through enhanced chemiluminescence using freshly prepared substrate solution based on 100 mM Tris (Tris-base, BP152Fisher Scientific) adjusted to pH 8.5 with Hydrochloric acid (A144S-212, Fisher), 1.2 mM Luminol (A8511, Sigma), 2.5 mM p-Coumaric acid (C9008, Sigma) and 0.04% Hydrogen peroxide (w/v, L14000, Alpha Aesar, Tewksbury, MA) on a G:BOX (Syngene, Frederick, MD) equipped with a Synoptics 4.2MP camera and controlled with Genesys software (Syngene). Protein bands were quantified by measuring peak areas using ImageJ [45]. The peak area for each protein was normalized against the peak area of a loading control. Raw data for western blots are provided in Supplementary Information.

To conduct immunoprecipitation, protein lysates were prepared in ice-cold Cell Lysis Buffer (9803, Cell Signaling) supplemented with Halt Protease and Phosphatase Inhibitor Cocktail (78442, Thermo Fisher Scientific). Cells were mechanically ruptured by pressing them through a PrecisionGlide needle (305109, BD Biosciences) for at least five times. Lysates were centrifuged and pellet at 4°C, and the supernatant was collected. The samples were incubated with Protein A Sepharose beads (50% bead slurry, 6501, BioVision) for 1 hr at 4°C to reduce non-specific binding. The samples were centrifuged and pelleted at 4°C, and the supernatant was collected and proceeded to immunoprecipitation. The supernatant was incubated with PFKP antibody (D4B2, Cell Signaling) and Protein A Sepharose beads (50% bead slurry) for overnight at 4°C with gentle rocking. Afterward, the samples were centrifuged at 4°C and the pellets were washed with cell lysis buffer for five times. The pellets were reconstituted in a Laemmli sample buffer with 2-mercaptoethanol, and boiled for 5 min before performing SDS-PAGE and immunoblotting.

Immunohistochemistry and image analysis.

The PFKP immunohistochemistry protein expression was determined in non-small cell lung carcinomas (NSCLC) from archived formalin-fixed paraffin-embedded (FFPE) tumors from patients that underwent surgical treatment between February 1999 and February 2012 at MD Anderson Cancer Center (Houston, Texas, USA). Tumor tissue was placed in a tissue microarray (TMA) using three 1-mm diameter core. This study was approved by the MD Anderson Cancer Center Institutional Review Board and was conducted according to the principles of the Helsinki Declaration.

Formalin-fixed and paraffin-embedded (FFPE) 4 μm thin tissue sections from the TMAs were used to perform immunohistochemistry in a Leica Bond Max automated stainer (Leica Biosystems GmbH, Nussloch, Germany). The tissue sections were deparaffinized and rehydrated following the Leica Bond protocol. Antigen retrieval was performed with Bond Solution #1 (Leica Biosystems, equivalent to citrate buffer, pH 6.0) for 20 min. The primary antibody (PFKP, mouse monoclonal antibody, dilution 1:2000, ThermoFisher Scientific, Catalog # MA5–25792) was incubated for 15 minutes at room temperature. The primary antibody was detected using the Bond Polymer Refine Detection kit (Leica Biosystems) with DAB as chromogen. The slides were counterstained with hematoxylin, dehydrated, and capped with coverslip. The antibody was tested for specificity using high and low expressing cell line pellets (HBEC76 PFKP overexpression and HBEC76 control cells, respectively). As a further negative control, regions of smooth muscle cells in the tissue slides were devoid of antibody, as expected.

The immunostained sections were digitally scanned using the Aperio AT2 slide scanner (Leica Biosystems) under 20x objective magnification. The scanned images were used to annotate different compartments: malignant cells, tumor stroma, non-tumoral stroma and normal bronchial epithelium. The compartmentalization was applied to each image. Stained nuclei were automatically detected by the software and nuclear regions were expanded to quantify cytoplasmic PFKP staining. This was followed by calculation of the percentage of cells with different levels of intensity of PFKP cytoplasmic expression: 0 (no staining), 1+ (weak staining), 2+ (moderate staining), or 3+ (strong staining). For this analysis, the "Cytonuclear v1.6" algorithm of the HALOv2.3 image analysis software (Indica Labs) was used under the supervision of a pathologist.

Protein mass spectrometry.

H2009 cells stably over-expressing TRIM21-GFP were washed once in ice-cold PBS, harvested and lysed in freshly prepared actin stabilization lysis buffer containing 50 mM KCl (Fisher, BP-366), 0.5% NP-40 (Fluka, 74385), 2 mM MgCl (Fisher, BP-214), 5 mM Tris-HCl (Fisher, BP-152), pH 7.5, 2mM ATP (Sigma, A2383), 10% glycerol (Fisher, BP-229), Alexa-Fluor-488-Phalloidin (0.3 U/ml, Invitrogen, A12379), cOmplete protease inhibitors (Roche, 11697498001) and phosphatase inhibitors [46], NaF(1 mM, Fisher, S299), Na-orthovanadate (1 mM, Fisher, S454), Na-pyrophosphate (10 mM, Sigma, 221368), Beta-glycerophosphate(1 mM, Sigma, G5422). Cells were lysed at 4°C rotating for 30 min and lysates were spun down at maximum speed in a table to centrifuge. The supernatant was collected and 30 μl anti GFP-agarose beads (GFP-nAb, Allele Biotechnology, San Diego,

CA) were added for 30 min rotating at 4°C. The beads were collected by centrifugation and washed 3 times with lysis buffer. The protein was eluted with 50 μl elution buffer (200 mM glycine, pH 2.5) and samples were spun in a microcentrifuge for one minute at 700 rpm. The supernatant was collected and neutralized with 5 μl neutralization buffer (1 M Tris base solution) according to manufacturer instructions. The sample was run into a 10% polyacrylamide gel for 10 min and stained with Aquastain blue (Bulldog Bio, AS001000) and de-stained in deionized water. The stained lane was cut into 1 mm cubes for mass-spectrometry.

Protein gel pieces were reduced and alkylated with DTT (20 mM) and iodoacetamide (27.5 mM). A 0.1 μg/μL solution of trypsin in 50 mM triethylammonium bicarbonate (TEAB) was added to completely cover the gel, allowed to sit on ice, and then 50 μL of 50 mM TEAB was added and the gel pieces were digested overnight (Pierce). Following solid-phase extraction cleanup with an Oasis HLB μelution plate (Waters), the resulting peptides were reconstituted in 10 uL of 2% (v/v) acetonitrile (ACN) and 0.1% trifluoroacetic acid in water. 2 uL of this were injected onto an Orbitrap Fusion Lumos mass spectrometer (Thermo Electron) coupled to an Ultimate 3000 RSLC-Nano liquid chromatography systems (Dionex). Samples were injected onto a 75 μm i.d., 75-cm long EasySpray column (Thermo), and eluted with a gradient from 1–28% buffer B over 90 min. Buffer A contained 2% (v/v) ACN and 0.1% formic acid in water, and buffer B contained 80% (v/v) ACN, 10% (v/v) trifluoroethanol, and 0.1% formic acid in water. The mass spectrometer operated in positive ion mode with a source voltage of 2.0 kV and an ion transfer tube temperature of 275 °C. MS scans were acquired at 120,000 resolution in the Orbitrap and up to 10 MS/MS spectra were obtained in the ion trap for each full spectrum acquired using higher-energy collisional dissociation (HCD) for ions with charges 2–7. Dynamic exclusion was set for 25 s after an ion was selected for fragmentation.

Raw MS data files were analyzed using Proteome Discoverer v2.2 (Thermo), with peptide identification performed using Sequest HT searching against the human protein database from UniProt. Fragment and precursor tolerances of 10 ppm and 0.6 Da were specified, and three missed cleavages were allowed. Carbamidomethylation of Cys was set as a fixed modification and oxidation of Met was set as a variable modification. The false-discovery rate (FDR) cutoff was 1% for all peptides.

Pulse chase protein stability analysis.

HEK cells were plated in 10-cm dishes and cultured until they became 80% confluent. Cells were then washed with warm PBS and conditioned in methionine-free DMEM (21013024, Thermo Fisher Scientific) for 1 hr at 37°C to deplete methionine reserves. To label (pulse) newly synthesized proteins, cells were cultured in methionine-free DMEM supplemented with Click-IT L-Azidohomoalanine (AHA, 25 μM; C10102, Thermo Fisher Scientific) for 12 hrs at 37°C. Once they were again washed with PBS, cells were either harvested in ice-cold RIPA buffer supplemented with Halt Protease and Phosphatase Inhibitor Cocktail (time zero-labeling control) or additionally cultured in methionine-containing DMEM for 24 hrs at 37°C (chase) before harvest. Cell lysates were mechanically ruptured, centrifuged, and quantified as mentioned above. The AHA-labeled proteins were derivatized using a Click-IT

Biotin Protein Analysis Detection Kit (C33372, Thermo Fisher Scientific) according to the manufacturer's instruction. In summary, azide-conjugated proteins were incubated with biotin-alkyne in the presence of copper sulfate for 20 min at room temperature to produce stable biotin-triazole-conjugated proteins. The samples were then proceeded to immunoprecipitate PFKP as stated above. Upon the completion of SDS-PAGE and western blotting, the labeled PFKP was detected using Streptavidin-POD Conjugate (11089153001, Roche, Basel, Switzerland).

Ubiquitination pull-down.

Ubiquitination of PFKP was detected using a Signal-Seeker Ubiquitination Detection Kit (BK161, Cytoskeleton, Denver, CO) according to the manufacturer's instruction. In summary, HEK cells were washed once in ice-cold PBS and collected in BlastR lysis buffer supplemented with De-ubiquitination/SUMOylation inhibitor (N-ethylmaleimide & TPEN, NEM09BB) and protease inhibitor cocktail (PIC02). Cell lysates were pre-cleaned using a BlastR filter and further diluted with BlastR Dilution Buffer. The samples were incubated with either control beads or ubiquitination affinity beads for 6 hrs at 4°C with gentle rocking. After washing the beads with BlastR-2 Wash Buffer for three times for 5 min each at 4°C, the beads were centrifuged and the pellets were incubated in Bead Elution Buffer for 5 min at room temperature. Once transferred and collected in the spin columns, 2-mercaptoethanol was added to the samples, which was then boiled for 5 min before running SDS-PAGE and western blot analysis.

Actin binding protein co-sedimentation.

Binding of TRIM21 to F-actin was detected using the Actin Binding Protein Spin-Down Biochem Kit (BK013, Cytoskeleton). HEK cells transiently over-expressing TRIM21-GFP, alpha-actinin 1-GFP or GFP alone were washed with ice-cold PBS and harvested in Cell Lysis Buffer (9803, Cell Signaling) supplemented with Halt Protease and Phosphatase Inhibitor Cocktail (78442, Thermo Fisher Scientific). After a freeze-thaw cycle in liquid nitrogen, the samples were centrifuged at 150,000 G using Optima MAX-XP Ultracentrifuge (393315, Beckman Coulter, Indianapolis, IN) for 2 hrs at 4°C to remove protein aggregates. The supernatants were collected and used for the actin binding assay. *In vitro* F-actin stock was prepared by reconstituting non-muscle actin (APHL99) with General Actin Buffer (BSA01–001) supplemented with ATP (0.2 mM, BSA04–001) and Actin Polymerization Buffer (BSA02–001) at room temperature for 1 hr, as instructed by the manufacturer. TRIM21-GFP, alpha-actinin 1-GFP, and GFP samples were incubated in the presence or absence of F-actin stock for 30 min at room temperature to facilitate F-actin binding. All samples were then centrifuged at 150,000 G for 2 hrs at 4°C. For each sample, the supernatant and the pellet were separately collected, reconstituted in Laemmli reducing-sample buffer, and boiled for 5 min before running SDS-PAGE and western blot analysis.

Immunofluorescence assay.

To assess TRIM21 distribution followed by the actinin-mediated enhancement of F-actin, HBEC76 cells were seeded on #1.5 cover glass (2850–22, Corning, Corning, NY). Immunofluorescence experiments were performed with standard protocols. In brief, cells were fixed with 4% paraformaldehyde (P6148, Sigma) in phosphate buffered saline (PBS)

for 10 min, washed and permeabilized with 0.5% Triton-X100 (BP151, Fisher) in PBS for 5 min. Cells were washed with PBS, blocked in PBS containing 5% goat serum (16210064, Thermo) for 1 hr at room temperature, and incubated with primary monoclonal mouse antibody specific for anti-Flag (F3165, Sigma) in PBS containing 5% goat serum for one hour at 4°C. Cells were washed and incubated with goat-anti-mouse antibody conjugated with Alexa-Fluor-568 for 30 min at room temperature. Cells were washed again and mounted with Vectashield antifade mounting medium (H-1000, Vector Labs, Burlingame, CA) for microscopy.

Bioinformatics analysis.

To demonstrate changes in expression in PFKP and E3 ligases of interest, level 3 RPKM normalized RNA sequencing data was downloaded from The Cancer Genome Atlas (TCGA Research Network: http://cancergenome.nih.gov/) from the following datasets: LUAD, lung adenocarcinoma; LUSC, lung squamous cell carcinoma; LUNG, total lung cancer. Heatmaps of the relative expression of E3 ligases were generated by normalizing individual gene expression values in tumor cells by their matched expression in normal cells and sorted by descending order. In order to further rank how consistently E3 ligases were downregulated across the 20 LCE datasets, 207 E3 ligase genes were selected and scored within the top 40 downregulated in cancer ligase genes. For the most consistent genes, shRNA vectors from the pGIPZ library were selected and stable HBEC knockdown cells were generated.

The sequences of all three isoforms of human PFK were aligned using FASTA on the Lalign website (https://embnet.vital-it.ch/software/LALIGN_form.html) [47]. Structural analysis of PFKP was conducted from the RCSB PDB (the Protein Data Bank: https://www.rcsb.org/) using the previously solved crystal structure of human phosphofructokinase-1 (PDB: 4XYK) [48].

To analyze the regulation of glycolysis in cancer, 63 genes involved in glucose metabolism were selected (Supplement table 8). From the Lung Cancer Explorer database (LCE, http://lce.biohpc.swmed.edu/lungcancer/) [29] the normalized expression data from 20 studies including 3159 samples were used (Supplement table 7). The gene expression from normal and cancer patients was averaged within studies and average values across all studies were plotted according to their ranked value cancer expression (Extended Data Fig. 1n, raw data Supplement table 8).

PFKs expression data in human bronchial epithelial cells was obtained from the BioGPS database(http://biogps.org) [49]. The structure of the PFKP tetramer was obtained from the RCSB Protein Data Bank, accession number 4XYK. Lysine residues of TRIM21 that were previously reported ubiquitinated were extracted from the phosphosite (https://www.phosphosite.org) database [37].

Analysis of cancer mutations in E3 ubiquitin ligases.

TRIM21 contains a RING type zinc finger domain that coordinates two zinc ions by eight cysteines and histidines (C1-C8), respectively and binds the E2 ligase. To identify TRIM21 cancer mutations that reduce E3 activity, the Catalogue of Somatic Mutations in Cancer database (COSMIC, https://cancer.sanger.ac.uk/cosmic) [50] and the cBioPortal for cancer

mutations [51,52] were searched for mutations around the conserved cysteines and histidines (see Supplement table 5, Extended Data Fig. 9a). Most prominently, the C54Y mutant exhibited strong protein aggregation (Extended Data Fig. 9f). A 161CA substitution was identified that resulted in a C54Y missense mutation in a hepatocellular carcinoma sample (Sample ID: COSM4912597). C54 is found at the eighth cysteine position C8 towards the C-terminal end of the domain. Cysteine to tyrosine mutations are observed with a single nucleotide substitution and may thus be found more frequently in cysteine rich zinc finger domains of the RING family E3 ubiquitin ligases. Because of their zinc ion binding role, they may be critical for protein activity and stability. Indeed, inactivation mutations in BRCA1 in RING domain C64Y at position C8 have been reported before [53–55]. To explore the relevance of RING domain CY mutations we searched COSMIC for a panel of RING domain E3 ubiquitin ligases extracted from the Universal Protein Resource (Uniprot, https://www.uniprot.org/) [56] (Supplement table 2). The amino acid changes were then analyzed in Excel software (Microsoft, Redmond, WA).

Flow cytometry.

Analysis and sorting were conducted on a FACS Aria II SORP flow cytometer (Beckton Dickinson, Franklin Lakes, NJ). Cells were resuspended in culture medium, filtered through a 40 μm cell strainer, and assessed with 488 nm excitation and with a 525 nm band pass filter. Prior to color analyses, cells were gated on the basis of forward and orthogonal light scatter. Fluorescence signals were measured with logarithmic amplifiers, and cells of interest were stringently sorted into a collection tube according to the spectral separation between the samples and control. Sorted cells were plated to a tissue culture dish for additional experiments.

Statistical analysis.

No statistical methods were used to predetermine sample size. The experiments were not randomized, and the investigators were not blinded to allocation during experiments and outcome assessment. An unpaired two-tailed Student's *t*-test was used for comparison between two groups. When the data points displayed a skewed distribution and failed a D'Agostrino-Pearson omnibus normality test, a two-tailed Mann-Whitney test was performed. If multiple groups were presented in a graph, one-way ANOVA was performed and, if significant, the Tukey test was also performed. All statistical analyses were performed using GraphPad Prism version 7.01 for Windows (GraphPad Software, La Jolla, CA, www.graphpad.com). All bar graphs show mean values with error bars (s.e.m. or s.d., as defined in figure legends). Precise *P* values are shown in the figures and, when appropriate, are rounded to the nearest a single significant digit. P values less than 1×10^{-4} are provided as a range. *P* values less than 0.05 are considered significant.
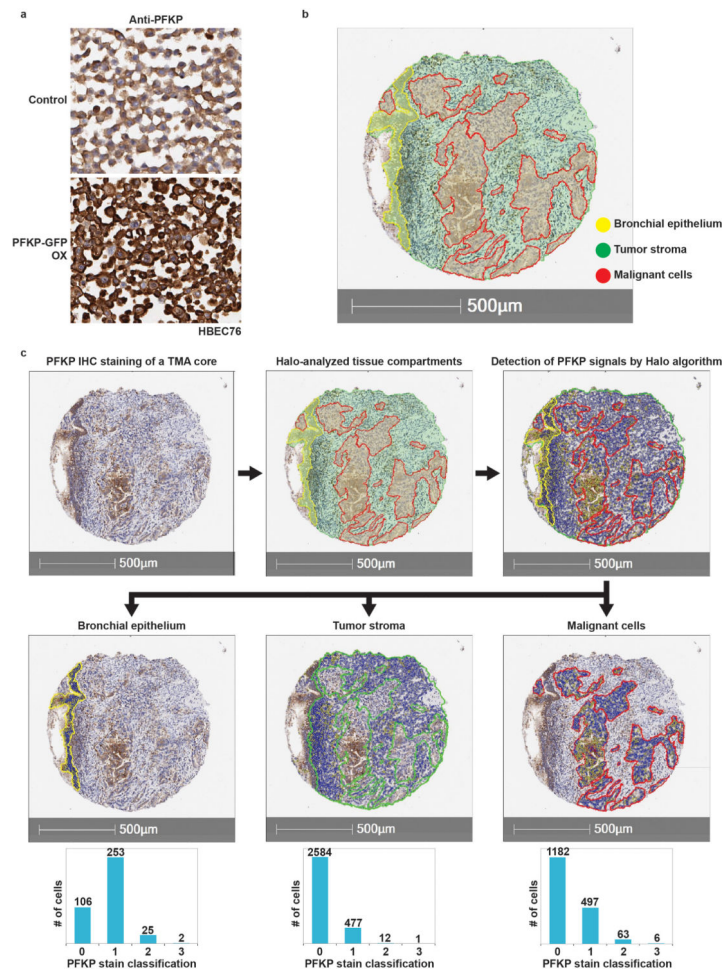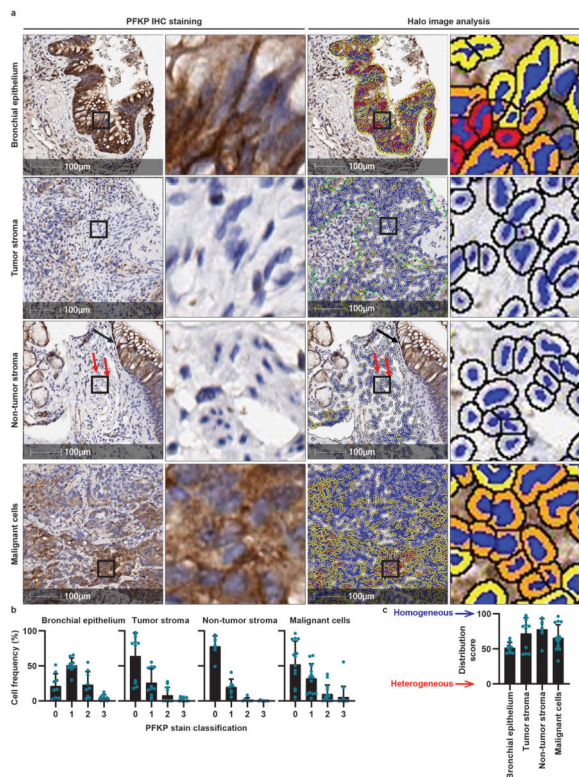
Extended Data
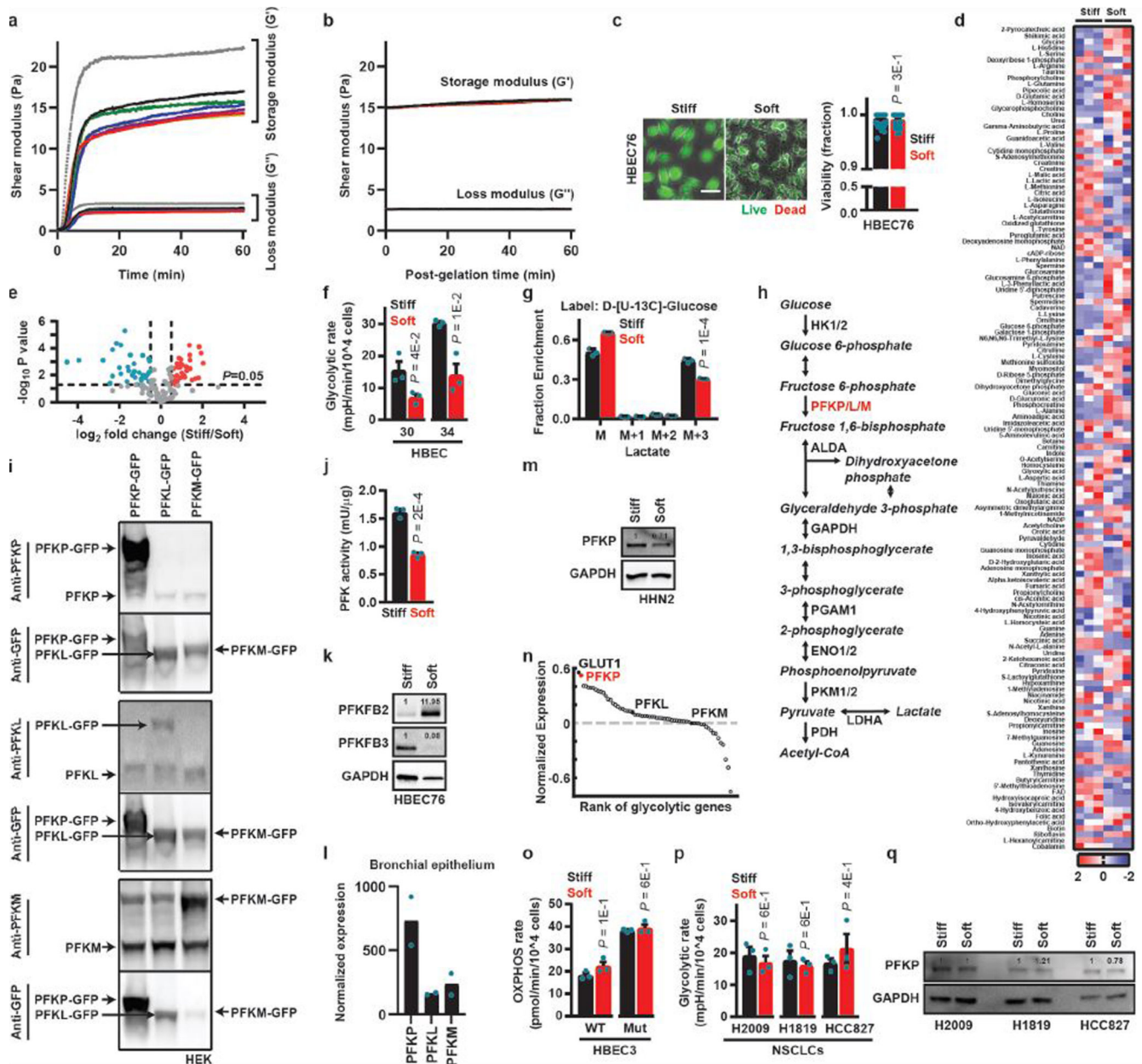
Extended Data Figure 1. Mechanical modulation of cell metabolism.
a, Shear moduli of soft substrates during liquid-to-solid gelation over the course of 60 min, shown as storage modulus (G') and loss modulus (G''). Time = 0 min indicates the start of the time sweep. The experiment was repeated 7 times over two separate days (distinct color for each experiment). **b**, Shear moduli of pre-formed soft substrates over the course of an additional 60 min, shown as storage modulus (G') and loss modulus (G''). Time = 0 min indicates the completion of 60 min of incubation at 37°C for gelation and the start of a second 60 min time sweep. The experiment was repeated twice (distinct color for each repeat). The shear modulus increased rapidly and reached a plateau within 5 min, with a 6-fold difference between storage modulus (G') and loss modulus (G''). Although the substrates are soft, this ratio indicates the formation of stable elastic hydrogels [36]. **c**, Left,

representative images of calcein AM (green) and ethidium homodimer (red) staining of HBEC76 on stiff and soft substrates. Scale bar, 50 μm. Right, fraction of calcein AM-positive cells relative to the combined count of calcein AM-positive and ethidium homodimer-positive cells on stiff (n = 50 images) and soft (n = 50) substrates from a single imaging experiment. Individual data points indicate fractions per image. **d**, Metabolomic profiling of HEBC76 on stiff and soft substrates (n = 3 independent cultures per substrate stiffness). Metabolic profiling was performed once. **e**, Volcano plot of metabolic shifts between substrates derived from Extended Data Fig. 1d. Each dot shows the average ratio in metabolite concentration between stiff and soft substrates vs. *P* values, based on three independent cultures. Vertical dotted line, $\log_2$ -fold change = ±0.5; horizontal dotted line, *P* value = 0.05). **f**, Glycolytic rates, normalized to cell number, of HBEC30 and 34 on stiff and soft substrates. **g**, Fraction enrichment of ^{13}C-labeled lactate synthesized from uniformly labeled D-^{13}C-glucose. M, no ^{13}C-labeling; M+1, one ^{13}C-labeling; M+2, two ^{13}C-labeling; M+3, three ^{13}C-labeling. Data are shown as mean ± s.e.m. of three independent experiments. **h**, Glycolytic pathway illustrating enzymes tested in Fig. 1d. PFKP, PFKL, and PFKM are highlighted in red. **i**, Verification of the specificity of PFK isoform-targeting (P, platelet; L, liver; M, muscle) antibodies. GFP-tagged PFK was expressed in HEK cells for each isoform and immunoblotting was performed. The experiment was performed once. **j**, PFK activity normalized by protein abundance on stiff and soft substrates. Data are shown as mean ± s.e.m. The experiment was performed once with three technical repeats per substrate stiffness. **k**, Abundance of PFKFB2 and PFKFB3 in HBEC76 per substrate stiffness. Representative data from three independent experiments. **l**, Normalized expression of PFKP, PFKL, and PFKM in human bronchial epithelium. Data of two replicates shown as the mean obtained from BioGPS: PFKP (#201037), PFKL (#201102), PFKM (#201102). **m**, Abundance of PFKP on stiff and soft substrates in head/neck epithelial cell line, HHN2. The experiment was performed once. **n**, Normalized expression of glycolytic genes ranked according to oncogenic enrichment. PFKP is highlighted in red; GLUT1, PFKL, and PFKM shown in black. **o**, Effect of oncogenic transformation of HBEC3 on oxidative phosphorylation (OXPHOS) rates on stiff and soft substrates. Data are normalized to cell number. **p**, Glycolytic rates, normalized to cell number, of NSCLCs (H2009, H1819, and HCC827) on stiff and soft substrates. **q**, Abundance of PFKP in H2009, H1819, and HCC827 on stiff and soft substrates. The experiment was performed once. Data in **f**, **o**, **p** are from three independent experiments, shown as mean ± s.e.m. Statistical significance was assessed using two-tailed Mann-Whitney test (**c**), unpaired multiple *t*-test (**e**) or two-tailed Student's *t*-test (**f**, **g**, **j**, **o**, **p**). Protein abundance was normalized to the abundance of GAPDH (**k**, **m**, **q**).

Extended Data Figure 2. Analytic workflow of immunohistochemistry (IHC) staining of PFKP.
a, HBEC76 cell pellets (control vs. PFKP-GFP overexpression) stained with PFKP antibody used for subsequent IHC analysis. The experiment was performed once. **b**, Microphotograph showing annotated areas of malignant cells (red), tumor stroma (green), and normal bronchial epithelium (yellow) using HALO v2.3 software in a tissue microarray (TMA) core of lung cancer tumor tissue. **c**, Microphotographs showing the workflow for image analysis using HALO v2.3 software. From left to right, top to bottom: PFKP staining in a TMA core with lung adenocarcinoma and bronchial epithelium; Halo mark-up image showing the compartments analyzed, bronchial epithelium in yellow, tumor stroma in green and malignant cells in red; Halo mark-up images showing the image analysis using the Halo algorithm to detect cells with PFKP cytoplasmic IHC expression per bronchial epithelium, tumor stroma, and malignant cells. Column charts show frequencies of different levels of expression (0, 1+, 2+, 3+) of PFKP per tissue type.

Extended Data Figure 3. IHC staining of PFKP in tissue microarray cores of lung cancer.
**a**, Microphotographs showing PFKP IHC immunohistochemistry and their respective image analysis performed in bronchial epithelium (8 cases; 9 cores), tumor stroma (5 cases; 11 cores), non-tumor stroma (5 cases; 7 cores), and malignant cells (6 cases; 14 cores). In non-tumor stroma, red arrows indicate smooth muscle and a black arrow indicates bronchial epithelium. Areas shown as an enlarged image are indicated by black squares. Single cell color outlines indicate Halo-analyzed PFKP expression (0, white; 1+, yellow, 2+, orange, 3+, red). Scale bar, 100 μm. The experiment was performed once. **b**, Frequency of cells for each PFKP staining classification (0, low to 3, high) analyzed from bronchial epithelium (8 cases; 9 cores), tumor stroma (5 cases; 11 cores), non-tumor stroma (5 cases; 7 cores), and malignant cells (6 cases; 14 cores). Individual dots represent data from a single core. Data are shown as mean ± s.d. **c**, Distribution score of PFKP staining analyzed from the panel **b**. The score was calculated for each core by subtracting the lowest frequency value from the highest frequency value. Values close to 100 (blue arrow) suggest a homogeneous (Dirac) distribution of PFKP staining while values close to 0 (red arrow) indicate a completely heterogeneous (uniform) distribution. Data are shown as mean ± s.d.
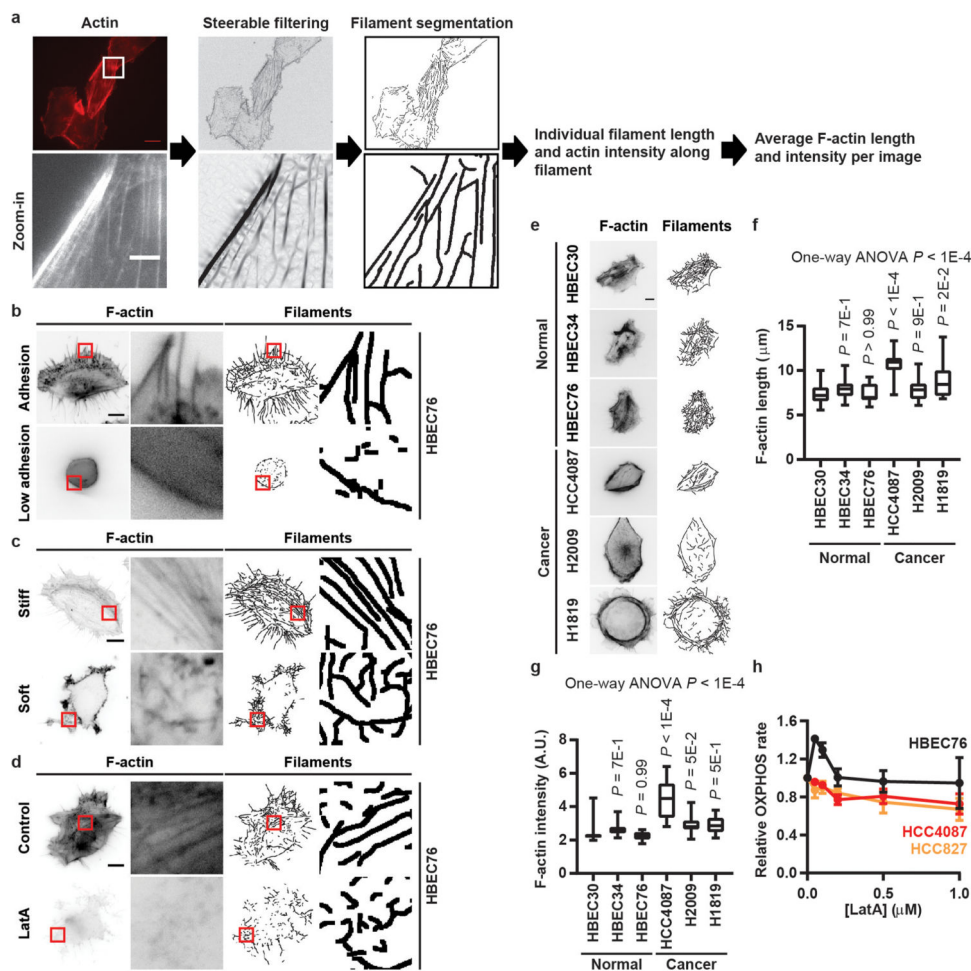
Extended Data Figure 4. Quantification of F-actin organization and relations to PFKP expression.

a, Image analysis pipeline to detect F-actin bundles. The core of the pipeline is a steerable filter that enhances the contrast of curvilinear image features. Zoom-in areas are shown in white and red squares. Scale bar, 20 μm or 5 μm (zoom-in). **b-d**, F-actin organization of HBEC76 and bundle detection after plating cells on normal adhesive and low adhesive substrates (**b**), on stiff and soft substrates (**c**) or after latrunculin A (LatA, 200 nM) treatment (**d**). Positions of zoom-ins are indicated by red boxes. Scale bar, 10 μm. Representative images from a single imaging experiment. **e**, F-actin organization of untransformed (normal) HBECs versus NSCLCs. Right panels show filament detection. Scale bar, 10 μm. Representative images from a single imaging experiment. Quantification of F-actin bundle length (**f**) or intensity (**g**) in HBECs (HBEC30, n = 21; HBEC34, n = 15; HBEC76, n = 16) versus NSCLCs (HCC4087, n = 11; H2009, n = 22; H1819, n = 11). **h**, Effect of latrunculin A treatment on oxidative phosphorylation of HBEC76 (black), HCC4087 (red), and HCC827 (orange). Mean oxidative phosphorylation rates normalized to control ± s.d. are shown for each group. Data are from three independent experiments. Data in **f**, **g** are shown as a box (median ± 25–75%) and whisker (max–min) plot, and statistical significance was assessed using one-way ANOVA and the Tukey test.
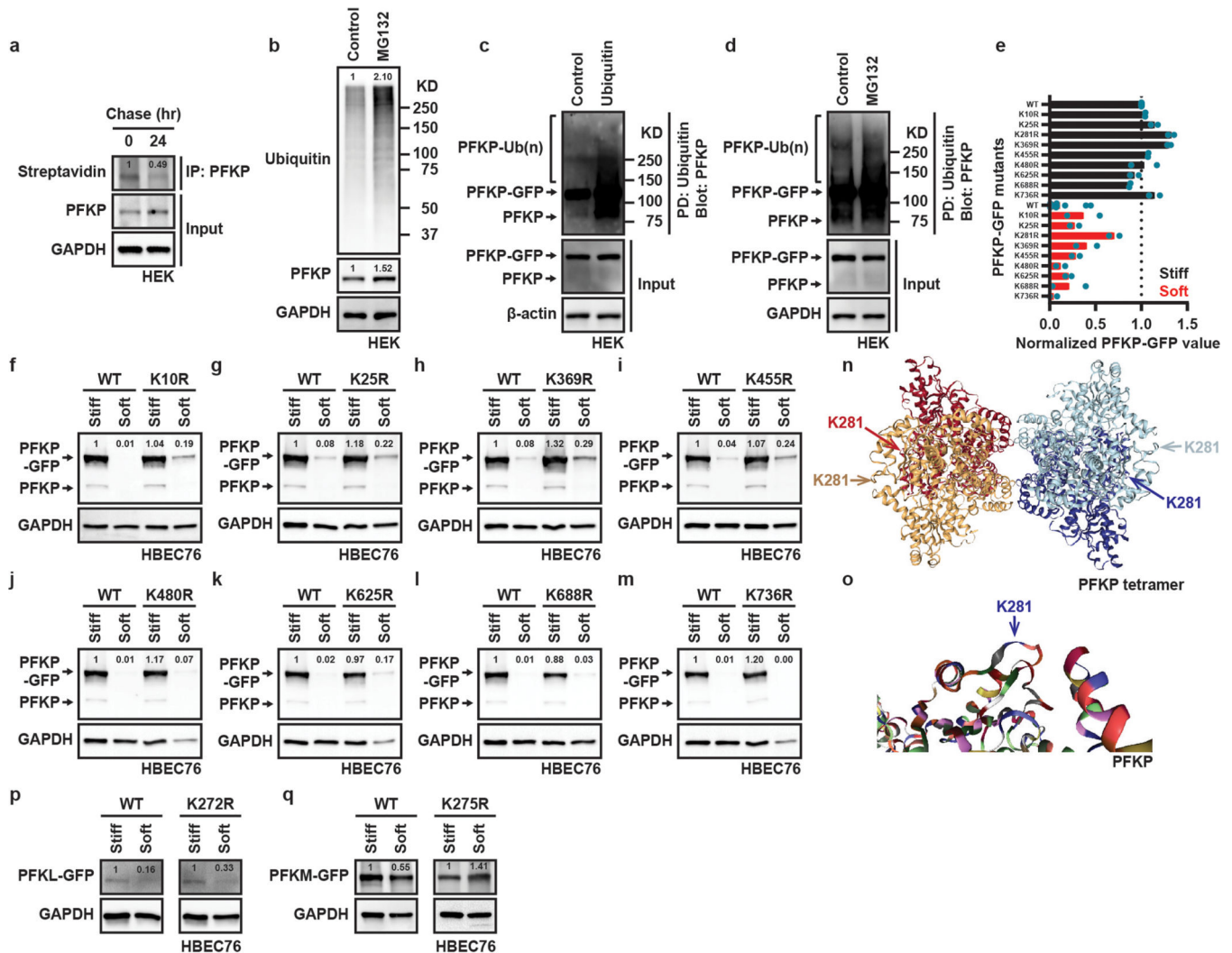
Extended Data Figure 5. PFKP ubiquitination and degradation.
a, Stability of PFKP analyzed by pulse chase experiments. HEK cells were pulsed with L-AHA for 12 hrs followed by a 0 or 24 hr chase period. The experiment was performed once. **b**, Abundance of ubiquitinated proteins and PFKP expression in HEK cells in the presence or absence of proteasome inhibitor MG132 (10 μM). Control, DMSO. Representative data from two independent experiments are shown. **c**, Abundance of polyubiquitinated PFKP upon ubiquitin pull-down using either control beads or beads conjugated to ubiquitin-binding protein using HEK cells. PD, pulldown. The experiment was performed once. **d**, Abundance of polyubiquitinated PFKP in the presence or absence of MG132 (10 μM for 3 hrs). Representative data from three independent experiments. **e**, Abundance of over-expressed PFKP-GFP harboring specified lysine-to-arginine (K-to-R) mutations on stiff and soft substrates. Data is normalized with respect to over-expressed wildtype (WT) PFKP-GFP on stiff substrate. Wildtype (n = 13) and each K-to-R mutants (n = 2). Data are shown as mean of two independent experiments. **f-m**, Abundance of PFKP-GFP harboring a lysine-to-arginine (K-to-R) mutation as indicated in cells cultured on stiff and soft substrates. Representative data from two independent experiments. **n**, Structure of a PFKP tetramer.

Each PFKP monomer is colored differently. Arrows point to the K281 sites in each monomer. **o**, Enlarged structural detail of PFKP around the K281 site. Each amino acid is shown in different color. **p**, Abundance of over-expressed PFKL-GFP harboring K272R mutation on stiff and soft substrates. The experiment was performed once. **q**, Abundance of over-expressed PFKM-GFP harboring K275R mutation on stiff and soft substrates. The experiment was performed once. In **a**, **b**, **d**, **f-m**, **p**, **q**, protein abundance was normalized to the abundance of GAPDH, and in **c** to the abundance of β-actin.

```
Alignment PFKP, PFKL, PFKM

sp|P17858|PFKAL_HUMAN    ---------MAAVDLEKLRASGAGKAIGVLTSGGDAQGMNAAVRAVTRMGIYVGAKVFLI
sp|P08237|PFKAM_HUMAN    MT---------HEEHHAAKTLGIGKAIAVLTSGGDAQGMNAAVRAVVRVGIFTGARVFFV
sp|Q01813|PFKAP_HUMAN    MDADDSRAPKGSLRKFLEHLSGAGKAIGVLTSGGDAQGMNAAVRAVVRMGIYVGAKVYFI
                                       :  *  *:**: .*************** .*:**:.:**:*::

sp|P17858|PFKAL_HUMAN    YEGYEGLVEGGENIKQANWLSVSNIIQLGGTIIGSARCKAFTTREGRRAAAYNLVQHGIT
sp|P08237|PFKAM_HUMAN    HEGYQGLVDGGDHIKEATWESVSMMLQLGGTVIGSARCKDFREREGRLAAAYNLVKRGIT
sp|Q01813|PFKAP_HUMAN    YEGYQGMVDGGSNIAEADWESVSSILQVGGTIIGSARCQAFRTREGRLKAACNLLQRGIT
                         :***:*:*.**.:* :* * *** ::*:***:******: *  **** ** **::::**

sp|P17858|PFKAL_HUMAN    NLCVIGGDGSLTGANIFRSEWGSLLEELVAEGKISETTARTYSHLNIAGLVGSIDNDFCG
sp|P08237|PFKAM_HUMAN    NLCVIGGDGSLTGADTFRSEWSDLLSDLQKAGKITDEEATKSSYLNIVGLVGSIDNDFCG
sp|Q01813|PFKAP_HUMAN    NLCVIGGDGSLTGANLFRKEWSGLLEELARNGQIDKEAVQKYAYLNVVGMVGSIDNDFCG
                         **************: **.**..**.:*   *:*.  . . ::**:.*:*********

sp|P17858|PFKAL_HUMAN    TDMTIGTDSALHRIMEVIDAITTTAQSHQRTFVLEVMGRHCGYLALVSALASGADWLFIP
sp|P08237|PFKAM_HUMAN    TDMTIGTDSALHRIMEIVDAITTTAQSHQRTFVLEVMGRHCGYLALVTSLSCGADWVFIP
sp|Q01813|PFKAP_HUMAN    TDMTIGTDSALHRIIEVVDAIMTTAQSHQRTFVLEVMGRHCGYLALVSALACGADWVFLP
                         **************:.:.*** *************************::*:.****:*:*

sp|P17858|PFKAL_HUMAN    EAPPEDGWENFMCERLGETRSRGSRLNIIIIAEGAIDRNGKPISSSYVKDLVVQRLGFDT
sp|P08237|PFKAM_HUMAN    ECPPDDDWEEHLCRRLSETRTRGSRLNIIIVAEGAIDKNGKPITSEDIKNLVVKRLGYDT
sp|Q01813|PFKAP_HUMAN    ESPPEEGWEEQMCVKLSENRARKKRLNIIIVAEGAIDTQNKPITSEKIKELVVTQLGYDT
                         *.**::.**: :* :*.*.*:* .******:****** :.:**:*. **:***.**:**

sp|P17858|PFKAL_HUMAN    RVTVLGHVQRGGTPSAFDRILSSKMGMEAVMALLEATPDTPACVVTLSGNQSVRLPLMEC
sp|P08237|PFKAM_HUMAN    RVTVLGHVQRGGTPSAFDRILGSRMGVEAVMALLEGTPDTPACVVSLSGNQAVRLPLMEC
sp|Q01813|PFKAP_HUMAN    RVTILGHVQRGGTPSAFDRILASRMGVEAVIALLEATPDTPACVVSLNGNHAVRLPLMEC
                         ***:*****************.*:**:***:****.*********:*.**:.********

sp|P17858|PFKAL_HUMAN    VQMTKEVQKAMDDKRFDEATQLRGGSFENNWNIYKLLAHQKPPKE--KSNFSLAILNVGA
sp|P08237|PFKAM_HUMAN    VQVTKDVTKAMDEKKFDEALKLRGRSFMNNWEVYKLLAHVRPPVS-KSGSHTVAVMNVGA
sp|Q01813|PFKAP_HUMAN    VQMTQDVQKAMDERRFQDAVRLRGRSFAGNLNTYKRLAIKLPDDQIPKTNCNVAVINVGA
                         **:*:::* ***:::*::::* :*** ** .*.: ** **  *  .  . . .:*::****

sp|P17858|PFKAL_HUMAN    PAAGMNAAVRSAVRTGISHGHTVYVVHDGFEGLAKGQVQEVGWHDVAGWLGRGGSMLGTK
sp|P08237|PFKAM_HUMAN    PAAGMNAAVRSTVRIGLIQGNRVLVVHDGFEGLAKGQIEEAGWSYVGGWTGQGGSKLGTK
sp|Q01813|PFKAP_HUMAN    PAAGMNAAVRSAVRVGIADGHRMLAIYDGFDGFAKGQIKEIGWTDVGGWTGQGGSILGTK
                         ***********:.**  *:  .:.:.***:*:****:.*:.*  .  :* *:** ***:*

sp|P17858|PFKAL_HUMAN    RTLPKGQLESIVENIRIYGIHALLVVGGFEAYEGVLQLVEARGRYEELCIVMCVIPATIS
sp|P08237|PFKAM_HUMAN    RTLPKKSFEQISANITKFNIQGLVIIGGFEAYTGGLELMEGRKQFDELCIPFVVIPATVS
sp|Q01813|PFKAP_HUMAN    RVLPGKYLEEIATQMRTHSINALLIIGGFEAYLGLLELSAAREKHEEFCVPMVMVPATVS
                         *.**   :*.*  ::   ..*:.*::******* * *:*  .* .::**:  : ::***:*

sp|P17858|PFKAL_HUMAN    NNVPGTDFSLGSDTAVNAAMESCDRIKQSASGTKRRVFIVETMGGYCGYLATVTGIAVGA
sp|P08237|PFKAM_HUMAN    NNVPGSDFSVGADTALNTICTTCDRIKQSAAGTKRRVFIIETMGGYCGYLATMAGLAAGA
sp|Q01813|PFKAP_HUMAN    NNVPGSDFSIGADTALNTITDTCDRIKQSASGTKRRVFIIETMGGYCGYLANMGGLAAGA
                         *****:***:*.:.***:*:   :*********:******:.***********.: *:*.**

sp|P17858|PFKAL_HUMAN    DAAYVFEDPFNIHDLKVNVEHMTEKMKTDIQRGLVLRNEKCHDYYTTEFLYNLYSSEGKG
sp|P08237|PFKAM_HUMAN    DAAYIFEEPFTIRDLQANVEHLVQKMKTTVKRGLVLRNEKCNENYTTDFIFNLYSEEGKG
sp|Q01813|PFKAP_HUMAN    DAAYIFEEPFDIRDLQSNVEHLTEKMKTTIQRGLVLRNESCSENYTTDFIYQLYSEEGKG
                         ****:**:** *:**:.****:.:***** ::******.* : ***:*:::**.****

sp|P17858|PFKAL_HUMAN    VFDCRTNVLGHLQQGGAPTPFDRNYGTKLGVKAMLWLSEKLREVYRKGRVFANAPDSACV
sp|P08237|PFKAM_HUMAN    IFDSRKNVLGHMQQGGSPTPFDRNFATKMGAKAMNWMSGKIKESYRNGRIFANTPDSGCV
sp|Q01813|PFKAP_HUMAN    VFDCRKNVLGHMQQGGAPSPFDRNFGTKISARAMEWITAKLKEARGRGKKFT-TDDSICV
                         :**.*.*****:****:*:*****:.** .:*::...** *:: *::*   .*: *: : ** **

sp|P17858|PFKAL_HUMAN    IGLKKKAVAFSPVTELKKDTDFEHRMPREQWWLSLRLMLKMLAQYRISMAAYVSGELEHV
sp|P08237|PFKAM_HUMAN    LGMRKRALVFQPVAELKDQTDFEHRIPKEQWWLKLRPILKILAKYEIDLDTSDHAHLEHI
sp|Q01813|PFKAP_HUMAN    LGISKRNVIFQPVAELRKQTDFEHRIPKEQWWLKLRPLMKILAKYRASYDVSDSGQLEHV
                         :*: *: : *.**:**:.:*****:*:*****.** ::*:**:*. . ..***:

sp|P17858|PFKAL_HUMAN    TRRTLSMDKGF
sp|P08237|PFKAM_HUMAN    TRKRSGEAAV-
sp|Q01813|PFKAP_HUMAN    QPWSV------
```
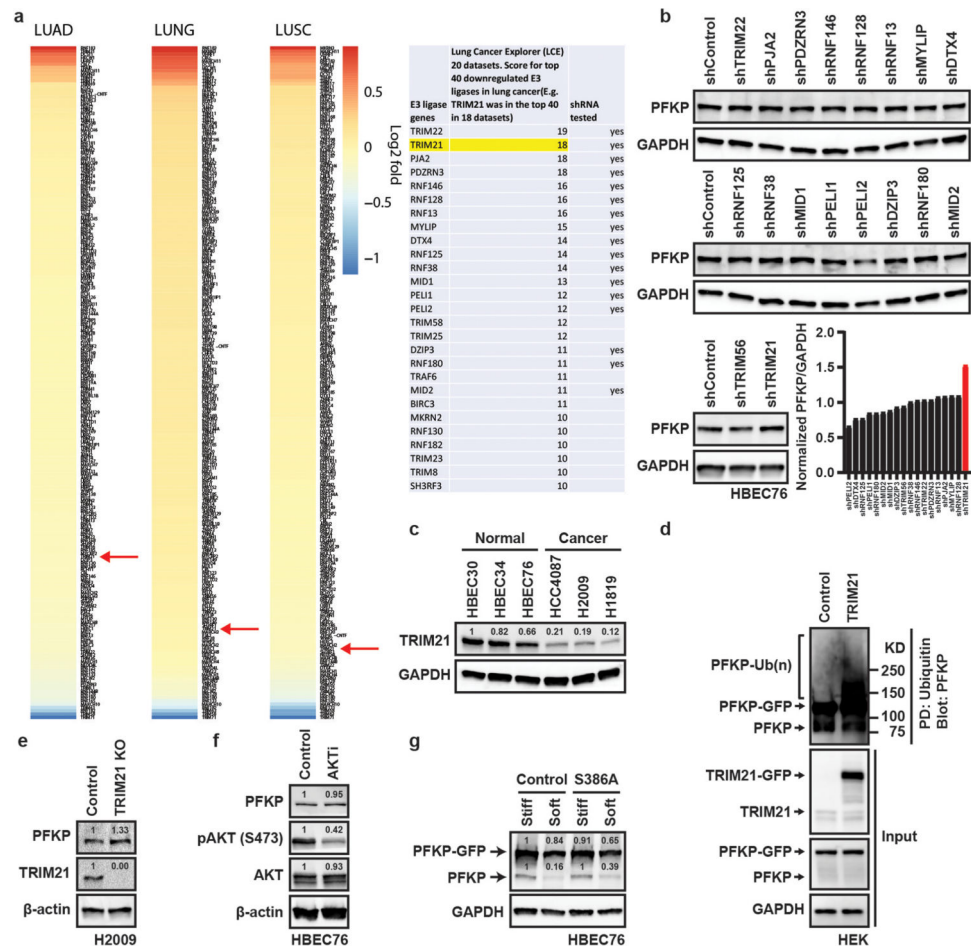
Extended Data Figure 6. Alignment of human PFK isoforms: PFKP, PFKL, and PFKM.
Conserved lysines are highlighted in green. Lysines reported as ubiquitinated in the Phosphosite database [37] are labeled in cyan. PFKP lysine site 281 is highlighted in red. The previously reported PFKP ubiquitination site, K10, is labeled in yellow [27].

a

LUAD   LUNG   LUSC

Log2 fold: 0.5 / 0 / −0.5 / −1

E3 ligase genes	Lung Cancer Explorer (LCE) 20 datasets. Score for top 40 downregulated E3 ligases in lung cancer (E.g. TRIM21 was in the top 40 in 18 datasets)	shRNA tested
TRIM22	19	yes
TRIM21	18	yes
PJA2	18	yes
PDZRN3	18	yes
RNF146	16	yes
RNF128	16	yes
RNF13	16	yes
MYLIP	15	yes
DTX4	14	yes
RNF125	14	yes
RNF38	14	yes
MID1	13	yes
PELI1	12	yes
PELI2	12	yes
TRIM58	12	
TRIM25	12	
DZIP3	11	yes
RNF180	11	yes
TRAF6	11	
MID2	11	yes
BIRC3	11	
MKRN2	10	
RNF130	10	
RNF182	10	
TRIM23	10	
TRIM8	10	
SH3RF3	10	

b

shControl, shTRIM22, shPJA2, shPDZRN3, shRNF146, shRNF128, shRNF13, shMYLIP, shDTX4 — PFKP / GAPDH

shControl, shRNF125, shRNF38, shMID1, shPELI1, shPELI2, shDZIP3, shRNF180, shMID2 — PFKP / GAPDH

shControl, shTRIM56, shTRIM21 — PFKP / GAPDH — HBEC76

Normalized PFKP/GAPDH (bar chart, 0 to 2.0)

c

Normal: HBEC30, HBEC34, HBEC76   Cancer: HCC4087, H2009, H1819

TRIM21   1   0.82   0.66   0.21   0.19   0.12

GAPDH

d

Control / TRIM21

PFKP-Ub(n), PFKP-GFP, PFKP — PD: Ubiquitin, Blot: PFKP — KD: 250, 150, 100, 75

TRIM21-GFP, TRIM21 — Input

PFKP-GFP, PFKP — Input

GAPDH — HEK

e

Control / TRIM21 KO

PFKP   1   1.33

TRIM21   1   0.00

β-actin — H2009

f

Control / AKTi

PFKP   1   0.95

pAKT (S473)   1   0.42

AKT   1   0.93

β-actin — HBEC76

g

Control / S386A — Stiff, Soft, Stiff, Soft

PFKP-GFP   1   0.84   0.91   0.65

PFKP   1   0.16   1   0.39

GAPDH — HBEC76

Extended Data Figure 7. TRIM21 as a downregulated E3 ligase in lung cancer.
a, Ranking of expression change of E3 ubiquitin ligases (n = 213 ligases) in lung cancer patients. LUAD, lung adenocarcinoma; LUSC, lung squamous cell carcinoma; LUNG, total lung cancer. Data were generated by normalizing individual expression of E3 ligases in tumor samples to their matched normal expression, as reported by the TCGA. Data is plotted in descending order on a $\log_2$ scale. TRIM21, red arrows. Right, a summary table of the ranked ligases is shown. Integrated from 20 datasets included in the Lung Cancer Explorer (LCE) [29]. Genes targeted by shRNA are indicated and TRIM21 is highlighted. **b**, Screening of 18 most consistently downregulated E3 ligases according to LCE for their effects on PFKP expression. Abundance of PFKP relative to GAPDH is summarized as a bar chart. The experiment was performed once. TRIM21, red, is the only of the tested ligases, whose depletion leads to an increase in PFKP expression. **c**, Abundance of TRIM21 in untransformed HBECs and NSCLCs. Representative data from two independent experiments are shown. **d**, Abundance of polyubiquinated PFKP in HEK cells without (control) and with overexpression of GFP-tagged TRIM21 (TRIM21-GFP). Representative data from two independent experiments. **e**, Abundance of PFKP in transformed H2009 cells upon CRISPR-based knockout (KO) of TRIM21. Representative data from two independent experiments. **f**, Abundance of PFKP after treating HBEC76 with AKT inhibitor X (AKTi, 10 μM) for 15 hrs. Representative data from two independent experiments. **g**, Abundance of
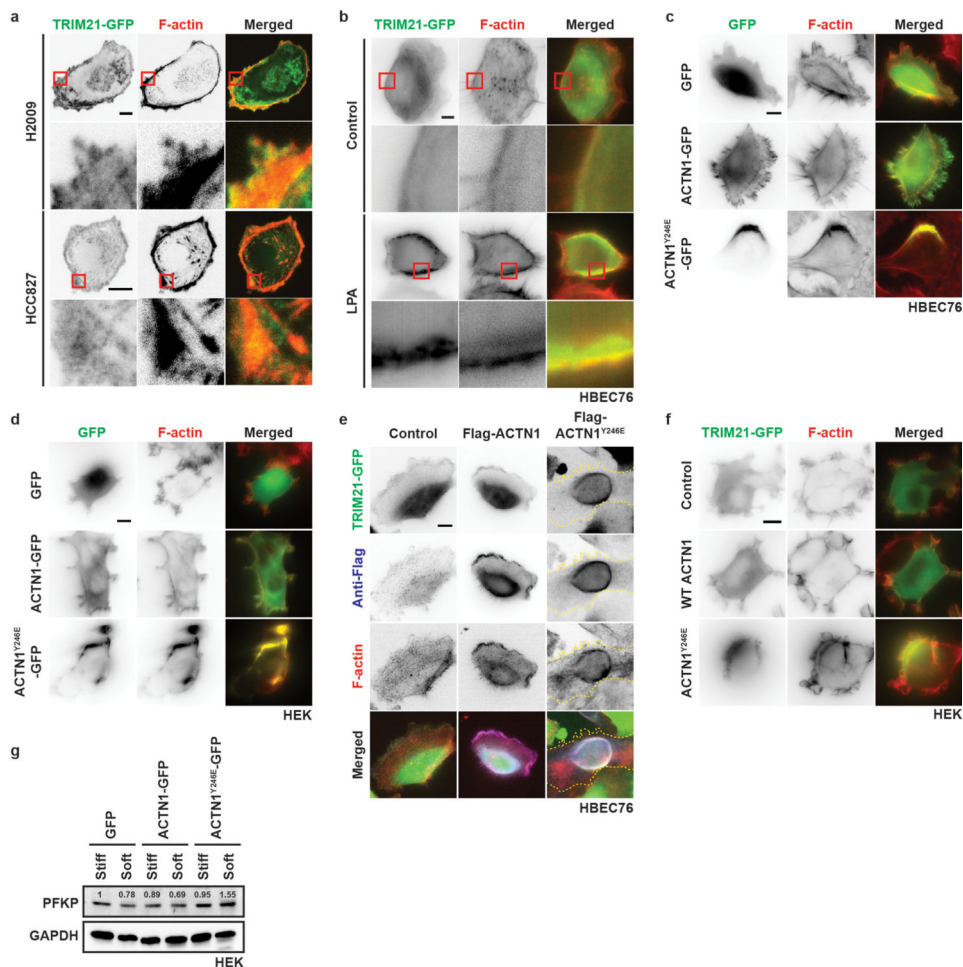
mutant PFKP-GFP (S386A), which cannot be phosphorylated by AKT, compared to control on stiff and soft substrates. The experiment was performed once. In **e**, **f**, protein abundance was normalized to the abundance of β-actin, and in **b**, **c**, **d**, **g** to the abundance of GAPDH.

Extended Data Figure 8. Effect of expression of phosphomimetic alpha-actinin 1^{Y246E} on F-actin organization and TRIM21 sequestration.

a, TIRF microscopy of TRIM21-GFP and F-actin in NSCLCs. Scale bar, 10 μm. Representative images from a single imaging experiment. **b**, Fluorescence microscopy of TRIM21-GFP and F-actin in HBEC76 treated with lysophosphatidic acid (LPA; 20 μM) for 30 min. Scale bar, 10 μm. Representative images from a single imaging experiment. **c**, Epi-fluorescence microscopy of HBEC76 expressing GFP alone, wildtype alpha-actinin 1 (ACTN1)-GFP or mutant alpha-actinin 1^{Y246E} (ACTN1^{Y246E})-GFP. Scale bar, 10 μm. Representative images from a single imaging experiment. **d**, Epi-fluorescence microscopy of HEK cells expressing GFP alone, ACTN1-GFP or mutant ACTN1^{Y246E}-GFP. Scale bar, 10 μm. Representative images from a single imaging experiment. **e**, Epi-fluorescence microscopy of TRIM21-GFP and F-actin following immunofluorescence labeling of Flag-tagged wildtype α-actinin 1 (WT ACTN1) or α-actinin 1 harboring the Y246E mutation (ACTN1^{Y246E}; the cell is outlined with a dotted yellow line) in HBEC76. Scale bar, 10 μm. Representative images from three independent experiments. **f**, Epi-fluorescence microscopy of TRIM21-GFP and F-actin upon over-expression of wildtype α-actinin 1 (WT ACTN1) or mutant α-actinin 1 (ACTN1^{Y246E}) in HEK cells. Scale bar, 10 μm. Representative images from a single imaging experiment. **g**, Abundance of PFKP on stiff and soft substrates upon over-expression of GFP alone, ACTN1-GFP or mutant ACTN1^{Y246E}-GFP in HEK cells.

Representative data from two independent experiments. Areas of zoom-in are indicated by red boxes (**a**, **b**). In all images (**a**-**f**), F-actin was stained with fluorescently conjugated phalloidin. Protein abundance was normalized by GAPDH (**g**).
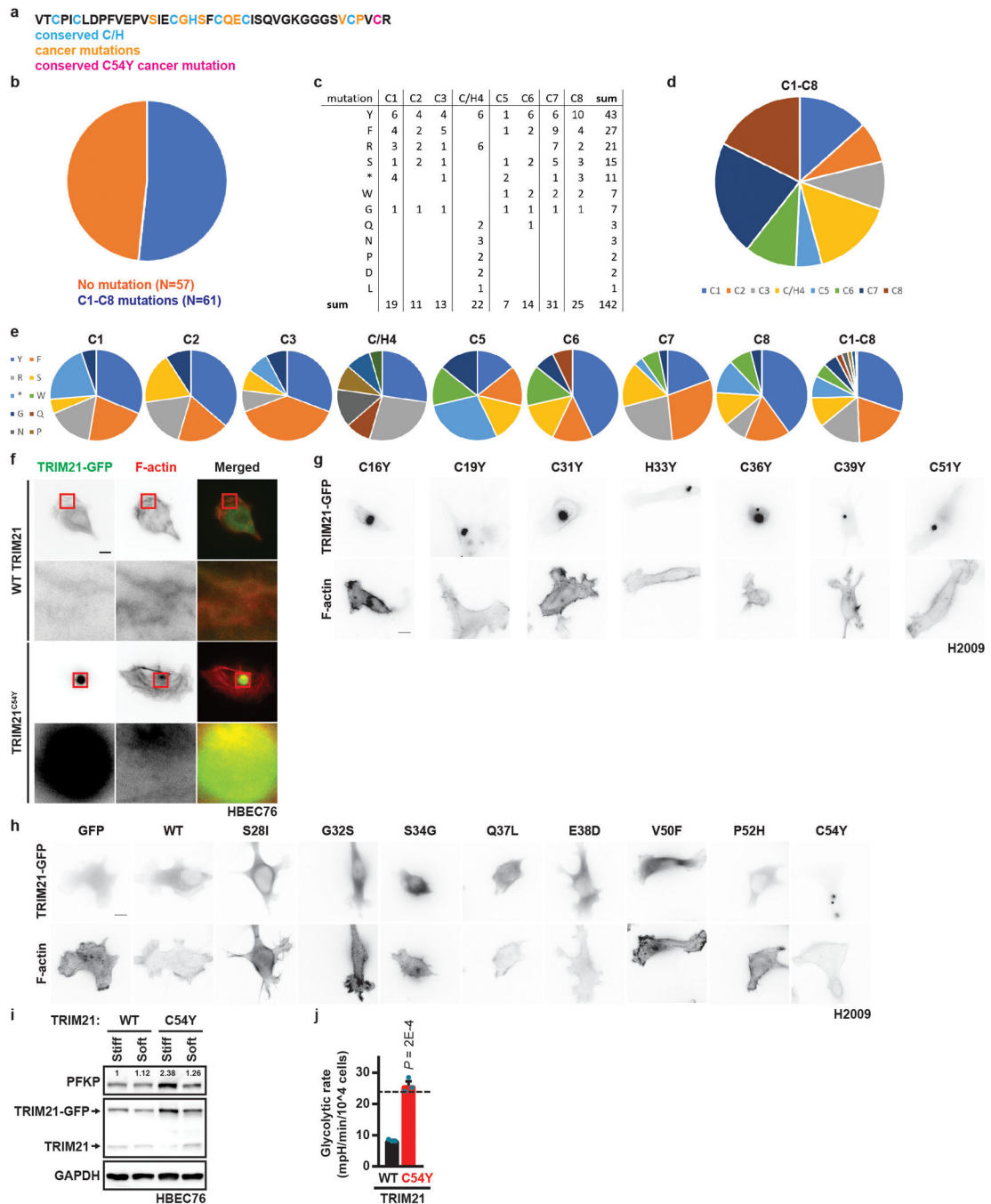
a

VTCPICLDPFVEPVSIECGHSFCQECISQVGKGGGSVCPVCR
conserved C/H
cancer mutations
conserved C54Y cancer mutation

b

No mutation (N=57)
C1-C8 mutations (N=61)

c

mutation	C1	C2	C3	C/H4	C5	C6	C7	C8	sum
Y	6	4	4	6	1	6	6	10	43
F	4	2	5			1	2	9	4	27
R	3	2	1	6			7	2	21
S	1	2	1		1	2	5	3	15
*	4		1		2		1	3	11
W					1	2	2	2	7
G	1	1	1		1	1	1	1	7
Q				2		1			3
N				3					3
P				2					2
D				2					2
L				1					1
sum	19	11	13	22	7	14	31	25	142

d C1-C8

C1 C2 C3 C/H4 C5 C6 C7 C8

e

C1 C2 C3 C/H4 C5 C6 C7 C8 C1-C8

Y F
R S
* W
G Q
N P

f

TRIM21-GFP F-actin Merged

WT TRIM21

TRIM21^C54Y

HBEC76

g

C16Y C19Y C31Y H33Y C36Y C39Y C51Y

TRIM21-GFP

F-actin

H2009

h

GFP WT S28I G32S S34G Q37L E38D V50F P52H C54Y

TRIM21-GFP

F-actin

H2009

i

TRIM21: WT C54Y
Stiff Soft Stiff Soft

PFKP 1 1.12 2.38 1.26
TRIM21-GFP →
TRIM21 →
GAPDH

HBEC76

j

Glycolytic rate (mpH/min/10^4 cells)

$P = 2E\text{-}4$

WT C54Y
TRIM21

Extended Data Figure 9. Analysis of somatic cancer mutations in RING domain E3 ubiquitin ligases.

a, Cancer mutations in TRIM21 RING domain found in proximity to conserved cysteines and histidines. **b**, Quantification of the number of genes that displayed one or more mutation at positions C1-C8 of the RING domain. **c**, Summary table of missense and nonsense mutations found in 118 genes at the conserved cysteine and histidine positions C1-C8. Amino acid code is tyrosine (Y), phenylalanine (F), arginine (R), serine (S), tryptophan (W), glycine (G), glutamine (Q), asparagine (N), proline (P), aspartic acid (D), leucine (L), stop

codon (*). **d**, Distribution of mutations across C1-C8. **e**, Frequency of missense and nonsense mutations at the position C1-C8 and overall. **f**, WT or mutant TRIM21^{C54Y}-GFP expression in HBEC76 counterstained for F-actin with phalloidin. Scale bar, 10 μm. Representative data from a single imaging experiment. **g**, Representative images of H2009 cells expressing GFP-tagged TRIM21 with indicated cysteine mutations and counterstained for F-actin with phalloidin. Scale bar, 10 μm. The experiment was performed once. **h**, Representative images of H2009 cells expressing GFP, GFP-tagged wildtype (WT) TRIM21 or TRIM21 with cancer-relevant mutations and counterstained for F-actin with phalloidin. Scale bar, 10 μm. The experiment was performed once. Mutations shown in (g) cause protein aggregation, whereas non-cysteine mutations in (h) do not. **i**, Abundance of PFKP on stiff and soft substrates when HBEC76 expressed WT or mutant TRIM21^{C54Y}-GFP. The experiment was performed once. **j**, Effect of expressing WT or mutant TRIM21^{C54Y} on glycolytic rates of HBEC76 normalized to cell number. Data are from three independent experiments shown as mean glycolytic rate ± s.e.m. Dotted line, glycolytic rates of HBEC76 on stiff substrates without over-expressing TRIM21 as indicated in Fig. 1d. Protein abundance was normalized by GAPDH (**i**).

Supplementary Material

Refer to Web version on PubMed Central for supplementary material.

Acknowledgements

REFERENCES

1. Liu Z et al. Mechanical tugging force regulates the size of cell-cell junctions. Proc Natl Acad Sci U S A 107, 9944–9949, doi:10.1073/pnas.0914547107 (2010). [PubMed: 20463286]

2. Vogel V & Sheetz M Local force and geometry sensing regulate cell functions. Nat Rev Mol Cell Biol 7, 265–275, doi:10.1038/nrm1890 (2006). [PubMed: 16607289]

3. Wang N, Butler JP & Ingber DE Mechanotransduction across the cell surface and through the cytoskeleton. Science 260, 1124–1127, doi:10.1126/science.7684161 (1993). [PubMed: 7684161]

4. Loisel TP, Boujemaa R, Pantaloni D & Carlier MF Reconstitution of actin-based motility of Listeria and Shigella using pure proteins. Nature 401, 613–616, doi:10.1038/44183 (1999). [PubMed: 10524632]

5. Kitamura K, Tokunaga M, Iwane AH & Yanagida T A single myosin head moves along an actin filament with regular steps of 5.3 nanometres. Nature 397, 129–134, doi:10.1038/16403 (1999). [PubMed: 9923673]

6. Engler AJ, Sen S, Sweeney HL & Discher DE Matrix elasticity directs stem cell lineage specification. Cell 126, 677–689, doi:10.1016/j.cell.2006.06.044 (2006). [PubMed: 16923388]

7. Discher DE, Janmey P & Wang YL Tissue cells feel and respond to the stiffness of their substrate. Science 310, 1139–1143, doi:10.1126/science.1116995 (2005). [PubMed: 16293750]

8. Geiger B, Bershadsky A, Pankov R & Yamada KM Transmembrane crosstalk between the extracellular matrix--cytoskeleton crosstalk. Nat Rev Mol Cell Biol 2, 793–805, doi:10.1038/35099066 (2001). [PubMed: 11715046]

9. Leckband DE, le Duc Q, Wang N & de Rooij J Mechanotransduction at cadherin-mediated adhesions. Curr Opin Cell Biol 23, 523–530, doi:10.1016/j.ceb.2011.08.003 (2011). [PubMed: 21890337]

10. Schlaepfer DD, Hanks SK, Hunter T & van der Geer P Integrin-mediated signal transduction linked to Ras pathway by GRB2 binding to focal adhesion kinase. Nature 372, 786–791 (1994). [PubMed: 7997267]

11. Burgstaller G et al. The instructive extracellular matrix of the lung: basic composition and alterations in chronic lung disease. Eur Respir J 50, doi:10.1183/13993003.01805-2016 (2017).

12. Vander Heiden MG, Cantley LC & Thompson CB Understanding the Warburg effect: the metabolic requirements of cell proliferation. Science 324, 1029–1033, doi:10.1126/science.1160809 (2009). [PubMed: 19460998]

13. Warburg O On the origin of cancer cells. Science 123, 309–314, doi:10.1126/science.123.3191.309 (1956). [PubMed: 13298683]

14. Christofk HR et al. The M2 splice isoform of pyruvate kinase is important for cancer metabolism and tumour growth. Nature 452, 230–233, doi:10.1038/nature06734 (2008). [PubMed: 18337823]

15. Sullivan WJ et al. Extracellular Matrix Remodeling Regulates Glucose Metabolism through TXNIP Destabilization. Cell, doi:10.1016/j.cell.2018.08.017 (2018).

16. Hu H et al. Phosphoinositide 3-Kinase Regulates Glycolysis through Mobilization of Aldolase from the Actin Cytoskeleton. Cell 164, 433–446, doi:10.1016/j.cell.2015.12.042 (2016). [PubMed: 26824656]

17. Bays JL, Campbell HK, Heidema C, Sebbagh M & DeMali KA Linking E-cadherin mechanotransduction to cell metabolism through force-mediated activation of AMPK. Nat Cell Biol 19, 724–731, doi:10.1038/ncb3537 (2017). [PubMed: 28553939]

18. Liu M, Tanswell AK & Post M Mechanical force-induced signal transduction in lung cells. Am J Physiol 277, L667–683 (1999). [PubMed: 10516207]

19. Bonnans C, Chou J & Werb Z Remodelling the extracellular matrix in development and disease. Nat Rev Mol Cell Biol 15, 786–801, doi:10.1038/nrm3904 (2014). [PubMed: 25415508]

20. Tanner LB et al. Four Key Steps Control Glycolytic Flux in Mammalian Cells. Cell Syst 7, 49–62 e48, doi:10.1016/j.cels.2018.06.003 (2018). [PubMed: 29960885]

21. Yalcin A, Telang S, Clem B & Chesney J Regulation of glucose metabolism by 6-phosphofructo-2-kinase/fructose-2,6-bisphosphatases in cancer. Exp Mol Pathol 86, 174–179, doi:10.1016/j.yexmp.2009.01.003 (2009). [PubMed: 19454274]

22. Uhlen M et al. Proteomics. Tissue-based map of the human proteome. Science 347, 1260419, doi:10.1126/science.1260419 (2015).

23. Kumar S & Weaver VM Mechanics, malignancy, and metastasis: the force journey of a tumor cell. Cancer Metastasis Rev 28, 113–127, doi:10.1007/s10555-008-9173-4 (2009). [PubMed: 19153673]

24. Sato M et al. Human lung epithelial cells progressed to malignancy through specific oncogenic manipulations. Mol Cancer Res 11, 638–650, doi:10.1158/1541-7786.MCR-12-0634-T (2013). [PubMed: 23449933]

25. Humphrey JD, Dufresne ER & Schwartz MA Mechanotransduction and extracellular matrix homeostasis. Nat Rev Mol Cell Biol 15, 802–812, doi:10.1038/nrm3896 (2014). [PubMed: 25355505]

26. Gan Z et al. Vimentin Intermediate Filaments Template Microtubule Networks to Enhance Persistence in Cell Polarity and Directed Migration. Cell Syst 3, 252–263 e258, doi:10.1016/j.cels.2016.08.007 (2016). [PubMed: 27667364]

27. Lee JH et al. Stabilization of phosphofructokinase 1 platelet isoform by AKT promotes tumorigenesis. Nat Commun 8, 949, doi:10.1038/s41467-017-00906-9 (2017). [PubMed: 29038421]

28. Pickart CM Mechanisms underlying ubiquitination. Annu Rev Biochem 70, 503–533, doi:10.1146/annurev.biochem.70.1.503 (2001). [PubMed: 11395416]

29. Cai L et al. LCE: an open web portal to explore gene expression and clinical associations in lung cancer. Oncogene 38, 2551–2564, doi:10.1038/s41388-018-0588-2 (2019). [PubMed: 30532070]

30. Shao H, Wu C & Wells A Phosphorylation of alpha-actinin 4 upon epidermal growth factor exposure regulates its interaction with actin. J Biol Chem 285, 2591–2600, doi:10.1074/jbc.M109.035790 (2010). [PubMed: 19920151]

31. Mertins P et al. Proteogenomics connects somatic mutations to signalling in breast cancer. Nature 534, 55–62, doi:10.1038/nature18003 (2016). [PubMed: 27251275]

32. Rikova K et al. Global survey of phosphotyrosine signaling identifies oncogenic kinases in lung cancer. Cell 131, 1190–1203, doi:10.1016/j.cell.2007.11.025 (2007). [PubMed: 18083107]

33. Wang C & Balch WE Bridging Genomics to Phenomics at Atomic Resolution through Variation Spatial Profiling. Cell Rep 24, 2013–2028 e2016, doi:10.1016/j.celrep.2018.07.059 (2018). [PubMed: 30134164]

34. Findlay GM et al. Accurate classification of BRCA1 variants with saturation genome editing. Nature 562, 217–222, doi:10.1038/s41586-018-0461-z (2018). [PubMed: 30209399]

35. Balch WE, Morimoto RI, Dillin A & Kelly JW Adapting proteostasis for disease intervention. Science 319, 916–919, doi:10.1126/science.1141448 (2008). [PubMed: 18276881]

Method References

36. Li L, Teller S, Clifton RJ, Jia X & Kiick KL Tunable mechanical stability and deformation response of a resilin-based elastomer. Biomacromolecules 12, 2302–2310, doi:10.1021/bm200373p (2011). [PubMed: 21553895]

37. Hornbeck PV et al. PhosphoSitePlus, 2014: mutations, PTMs and recalibrations. Nucleic Acids Res 43, D512–520, doi:10.1093/nar/gku1267 (2015). [PubMed: 25514926]

38. Zacharias DA, Violin JD, Newton AC & Tsien RY Partitioning of lipid-modified monomeric GFPs into membrane microdomains of live cells. Science 296, 913–916, doi:10.1126/science.1068539 (2002). [PubMed: 11988576]

39. Ran FA et al. Genome engineering using the CRISPR-Cas9 system. Nat Protoc 8, 2281–2308, doi:10.1038/nprot.2013.143 (2013). [PubMed: 24157548]

40. Zerbino DR et al. Ensembl 2018. Nucleic Acids Res 46, D754–D761, doi:10.1093/nar/gkx1098 (2018). [PubMed: 29155950]

41. Mullen AR et al. Oxidation of alpha-ketoglutarate is required for reductive carboxylation in cancer cells with mitochondrial defects. Cell Rep 7, 1679–1690, doi:10.1016/j.celrep.2014.04.037 (2014). [PubMed: 24857658]

42. Chong J et al. MetaboAnalyst 4.0: towards more transparent and integrative metabolomics analysis. Nucleic Acids Res 46, W486–W494, doi:10.1093/nar/gky310 (2018). [PubMed: 29762782]

43. Mullen AR et al. Reductive carboxylation supports growth in tumour cells with defective mitochondria. Nature 481, 385–388, doi:10.1038/nature10642 (2011). [PubMed: 22101431]

44. Edelstein A, Amodaj N, Hoover K, Vale R & Stuurman N Computer control of microscopes using microManager. Curr Protoc Mol Biol Chapter 14, Unit14 20, doi:10.1002/0471142727.mb1420s92 (2010).

45. Schneider CA, Rasband WS & Eliceiri KW NIH Image to ImageJ: 25 years of image analysis. Nat Methods 9, 671–675 (2012). [PubMed: 22930834]

46. Wilson-Grady JT, Haas W & Gygi SP Quantitative comparison of the fasted and re-fed mouse liver phosphoproteomes using lower pH reductive dimethylation. Methods 61, 277–286, doi:10.1016/j.ymeth.2013.03.031 (2013). [PubMed: 23567750]

47. Pearson WR Rapid and sensitive sequence comparison with FASTP and FASTA. Methods Enzymol 183, 63–98 (1990). [PubMed: 2156132]

48. Webb BA et al. Structures of human phosphofructokinase-1 and atomic basis of cancer-associated mutations. Nature 523, 111–114, doi:10.1038/nature14405 (2015). [PubMed: 25985179]

49. Wu C, Jin X, Tsueng G, Afrasiabi C & Su AI BioGPS: building your own mash-up of gene annotations and expression profiles. Nucleic Acids Res 44, D313–316, doi:10.1093/nar/gkv1104 (2016). [PubMed: 26578587]

50. Forbes SA et al. COSMIC: somatic cancer genetics at high-resolution. Nucleic Acids Res 45, D777–D783, doi:10.1093/nar/gkw1121 (2017). [PubMed: 27899578]

51. Gao J et al. Integrative analysis of complex cancer genomics and clinical profiles using the cBioPortal. Sci Signal 6, pl1, doi:10.1126/scisignal.2004088 (2013).

52. Cerami E et al. The cBio cancer genomics portal: an open platform for exploring multidimensional cancer genomics data. Cancer Discov 2, 401–404, doi:10.1158/2159-8290.CD-12-0095 (2012). [PubMed: 22588877]

53. Ruffner H, Joazeiro CA, Hemmati D, Hunter T & Verma IM Cancer-predisposing mutations within the RING domain of BRCA1: loss of ubiquitin protein ligase activity and protection from radiation hypersensitivity. Proc Natl Acad Sci U S A 98, 5134–5139, doi:10.1073/pnas.081068398 (2001). [PubMed: 11320250]

54. Rummel S, Varner E, Shriver CD & Ellsworth RE Evaluation of BRCA1 mutations in an unselected patient population with triple-negative breast cancer. Breast Cancer Res Treat 137, 119–125, doi:10.1007/s10549-012-2348-2 (2013). [PubMed: 23192404]

55. Fackenthal JD et al. High prevalence of BRCA1 and BRCA2 mutations in unselected Nigerian breast cancer patients. Int J Cancer 131, 1114–1123, doi:10.1002/ijc.27326 (2012). [PubMed: 22034289]

56. UniProt Consortium, T. UniProt: the universal protein knowledgebase. Nucleic Acids Res 46, 2699, doi:10.1093/nar/gky092 (2018). [PubMed: 29425356]
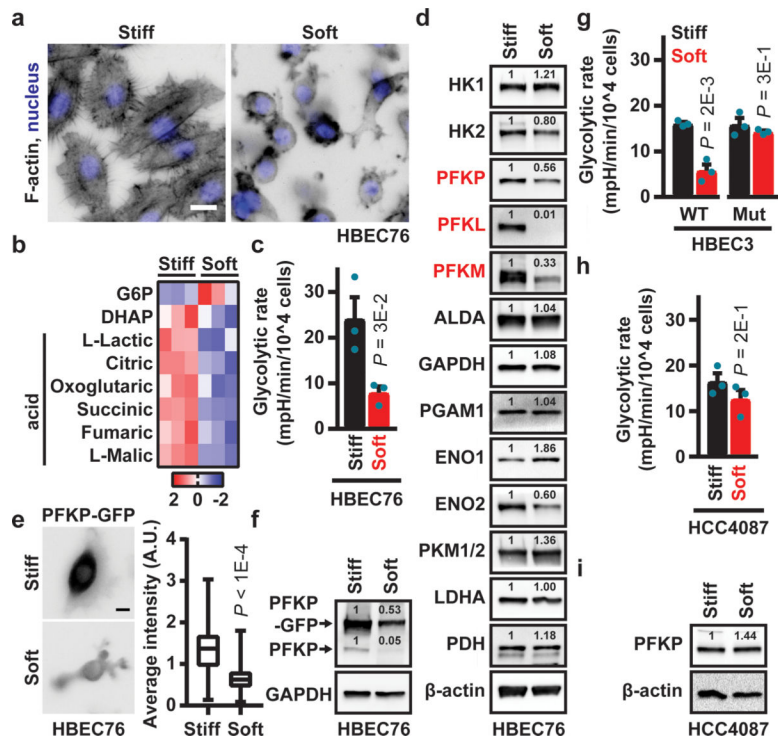
Figure 1. Glycolysis is mechanically modulated.
a, Morphological differentiation of human bronchial epithelial cells (HBEC76) on stiff and soft substrates. F-actin, grey; nuclei, blue. Scale bar, 15 μm. Representative images from three independent experiments. **b**, Relative abundance of glucose-derived metabolites on stiff and soft substrates in a heatmap (n = 3 independent cultures); red, accumulation; blue, depletion. Metabolic profiling was performed once. G6P, glucose 6-phosphate; DHAP, dihydroxyacetone phosphate. **c**, Glycolytic rates of HBEC76 normalized to cell number on stiff and soft substrates. **d**, Abundance of glycolytic enzymes on stiff and soft substrates: HK1, hexokinase 1; HK2, hexokinase 2; PFKP, phosphofructokinase platelet; PFKL, phosphofructokinase liver; PFKM, phosphofructokinase muscle; ALDA, aldolase A; GAPDH, glyceraldehyde 3-phosphate dehydrogenase; PGAM1, phosphoglycerate mutase 1; ENO1, enolase 1; ENO2, enolase 2; PKM½, pyruvate kinase M1/M2; LDHA, lactate dehydrogenase A; PDH, pyruvate dehydrogenase. Representative data from two independent experiments. **e**, Left, Representative images of HBEC76 overexpressing GFP-tagged PFKP (PFKP-GFP) on soft and stiff substrates. Scale bar, 10 μm. Right, average PFKP-GFP intensity on stiff (n = 55 cells) and soft (n = 61) substrates from a single imaging experiment. Data shown as a box (median ± 25–75%) and whisker (max–min) plot. **f**, PFKP-GFP and PFKP abundance on stiff and soft substrates. Representative data from two independent experiments are shown. **g**, Glycolytic rates of wildtype (WT) and mutant (Mut; sh-p53, KRAS^{V12}, c-MYC) HBEC3 normalized to cell number. **h**, Glycolytic rates of HCC4087 on stiff and soft substrates normalized to cell number. **i**, Abundance of PFKP in HCC4087 on stiff and soft substrates. Representative data from two independent experiments are shown. In **c**, **g**, **h**, data from three independent experiments are shown (dots); bar graph indicates mean ± s.e.m. of repeats. Statistical significance was assessed
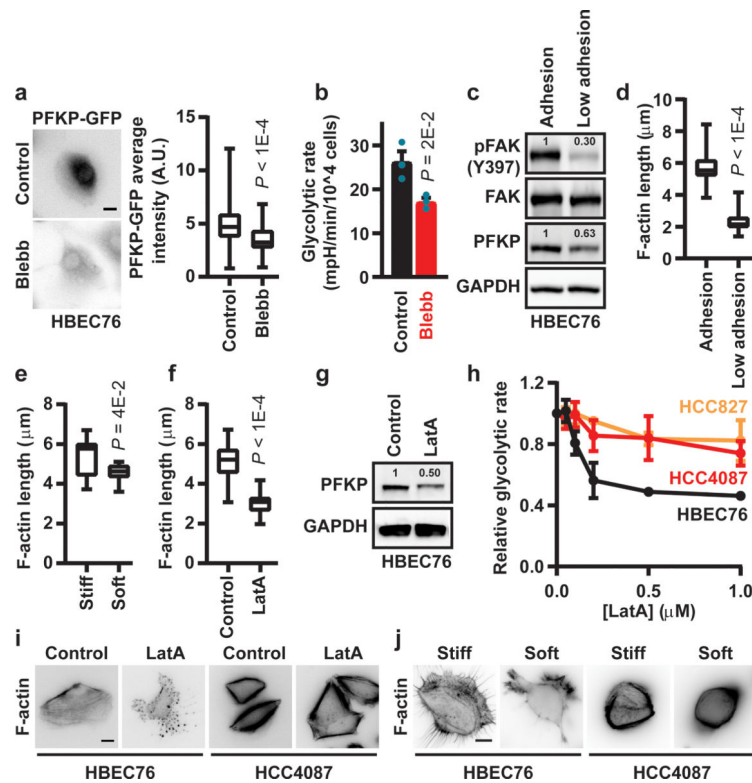
using two-tailed Student's *t*-test (**c**, **g**, **h**) or two-tailed Mann-Whitney test (**e**). Protein abundance was normalized to the abundance of β-actin (**d**, **i**) or GAPDH (**f**).

Figure 2. F-actin bundling enhances glycolysis.
a, Over-expression of PFKP-GFP in HBEC76 under pharmacological perturbation of myosin II. Control, DMSO; Blebb, blebbistatin (50 μM). Scale bar, 10 μm. Left, representative images. Right, box plots of the distribution of per-cell average intensity of PFKP-GFP under DMSO (control, n = 55 cells) and blebbistatin (n = 51) treatment from a single imaging experiment. **b**, Effect of same treatments on glycolytic rates of HBEC76 normalized to cell number. Data from three independent experiments are shown (dots); bar graph indicates mean ± s.e.m. of repeats. **c**, Abundance of PFKP, phosphorylated FAK (pFAK, Y397), and total FAK upon HBEC76 culture on normal adhesive versus low adhesive substrates. Representative data from three independent experiments are shown. **d-f**, Length of F-actin bundles in HBEC76 plated on normal adhesive (n = 45 cells) versus low adhesive (n = 30) substrates (**d**), on stiff (n = 10) versus soft (n = 14) substrates (**e**), and under DMSO (n = 50) versus latrunculin A (LatA, 200 nM; n = 50) treatment (**f**). Bundle lengths were averaged per cell and distributions of the cell population from a single imaging experiment displayed as whisker plots. **g**, Abundance of PFKP upon LatA treatment. Control, DMSO. Representative data from three independent experiments are shown. **h**, Glycolytic response to increasing dose of LatA in HBEC76 (black), HCC4087 (red), and HCC827 (orange). Mean glycolytic rates normalized to control ± s.d. are shown for each concentration. Data are from three independent experiments. **i**, Representative fluorescence images of F-actin organization in HBEC76 and HCC4087 after LatA treatment vs. DMSO control from two independent experiments. Scale bar, 10 μm. **j**, Representative fluorescence images of F-actin organization in HBEC76 and HCC4087 on stiff and soft substrates from two independent experiments. Scale bar, 10 μm. Data in **a**, **d-f** are shown as a box (median ± 25–75%) and whisker (max–min) plot. Statistical significance was assessed using two-tailed
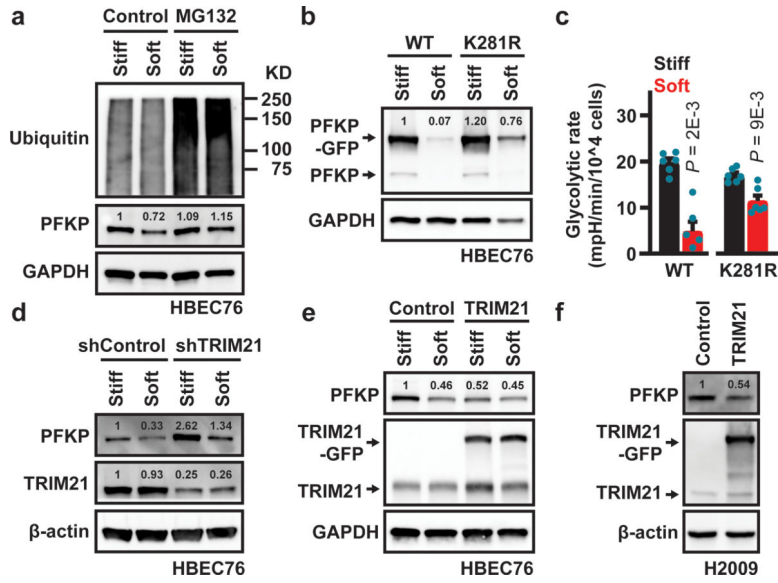
Student's *t*-test (**b**) or two-tailed Mann-Whitney test (**a**, **d-f**). Protein abundance was normalized to the abundance of GAPDH (**c**, **g**).

Figure 3. TRIM21 mediates mechanically modulated PFKP degradation.

a, Abundance of PFKP and ubiquitination in HBEC76 on stiff and soft substrates in the presence or absence of proteasome inhibitor MG132. Representative data from three independent experiments. **b**, Abundance of wildtype or mutant PFKP-GFP harboring K281R mutation (selected from Extended Data Fig. 5e) on stiff and soft substrates. Representative data from two independent experiments. **c**, Glycolytic rates, normalized to cell number, of HBEC76 expressing wildtype or K281R mutant PFKP on stiff and soft substrates (n = 6 independent cultures for each condition) from a single experiment. Bar graph indicates mean ± s.e.m. **d**, Abundance of PFKP in HBEC76 on stiff and soft substrates upon TRIM21 shRNA knockdown (shTRIM21). Representative data from two independent experiments. **e**, Abundance of PFKP in HBEC76 on stiff and soft substrates upon TRIM21-GFP over-expression. Representative data from two independent experiments. **f**, Abundance of PFKP in transformed H2009 cells upon TRIM21-GFP over-expression. Representative data from two independent experiments. Statistical significance was assessed using two-tailed Mann-Whitney test (**c**). Protein abundance was normalized to the abundance of GAPDH (**a**, **b**, **e**) or β-actin (**d**, **f**).
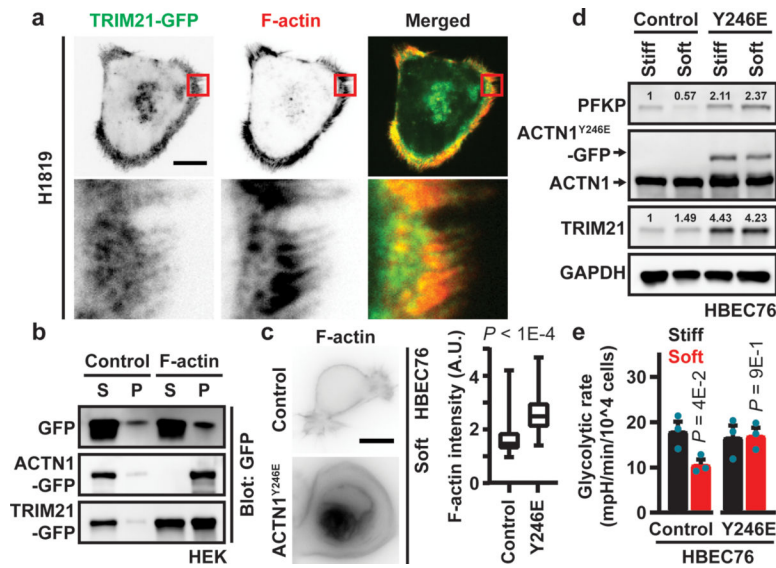
Figure 4. TRIM21's E3 ligase activity is negatively regulated by sequestration on F-actin bundles.

a, TIRF microscopy of TRIM21-GFP and F-actin in H1819. Scale bar, 10 μm. Red squares, areas of zoom-in. Representative images from a single imaging experiment. Experiments using other NSCLCs are shown in Extended Data Fig. 8a. **b**, Co-sedimentation of F-actin with TRIM21-GFP, α-actinin 1 (ACTN1)-GFP (positive control), and GFP (negative control) collected from HEK cell lysates. S, supernatant; P, pellet. Representative data from two independent experiments. **c**, Left, representative images of HBEC76 expressing WT ACTN1 (control) or mutant ACTN1^{Y246E} stained for F-actin with Alexa-Fluor-568 conjugated phalloidin on soft substrates. Scale bar, 10 μm. Right, average intensity of F-actin for control (50 cells) and ACTN1^{Y246E} expression (n = 50 cells) from a single imaging experiment. Data shown as a box (median ± 25–75%) and whisker (max–min) plot. **d**, Abundance of PFKP on stiff and soft substrates upon over-expression of WT ACTN1 (control) or ACTN1^{Y246E} in HBEC76. Representative data from two independent experiments. Replicated experiments using HEK cells are shown in Extended Data Fig. 8g. **e**, Glycolytic rates, normalized to cell number, of HBEC76 expressing WT ACTN1 (control) or ACTN1^{Y246E} on stiff and soft substrates. Data from three independent experiments are shown as mean glycolytic rate ± s.e.m. Statistical significance was assessed using two-tailed Mann-Whitney test (**c**) or two-tailed Student's *t*-test (**e**). Protein abundance was normalized to the abundance of GAPDH (**d**).